TECHNISCHE UNIVERSITÄT MÜNCHEN

Fakultät für Medizin

Implementation of MRI based methods for the non-invasive characterization of pancreatic ductal adenocarcinoma in mice

Florian Alexander Englert

Vollständiger Abdruck der von der Fakultät für Medizin zur Erlangung des akademischen Grades eines Doktors der Medizin genehmigten Dissertation.

Vorsitzender: Prof. Dr. Florian Eyer

Prüfende/-r der Dissertation:

1. Prof. Dr. Rickmer Braren

2. apl. Prof. Dr. Hans-Dieter Allescher

Die Dissertation wurde am 02.09.2021 bei der Technischen Universität München eingereicht und durch die Fakultät für Medizin am 17.05.2022 angenommen.

Abstract

Given its increasing incidence, imaging-based classification of pancreatic ductal adenocarcinoma (PDAC) has emerged as a crucial need in PDAC research. One hallmark of the condition is the genetic and morphologic heterogeneity that determines, amongst other factors, resistance to treatment and aggressiveness of this cancer. In recent years, different approaches have attempted to understand and describe this complexity of PDAC – in particular through molecular and structural stratification into defined subtypes. Today, classical- (epithelial) and quasi-mesenchymal (basal-like, squamos) subtypes are identified and correlated to benefit survival and better therapy response of these subtypes to FOLFIRINOX and Gemcitabine / Abraxane respectively.

Nuclear magnetic resonance (NMR) is based on the quantum mechanical interaction between nuclear spins, magnetic fields and radio waves. Dynamic nuclear spin polarization (DNP) paved the way for performing NMR in liquids by bringing nuclear spins into a hyperpolarized state and thereby amplifying the measurable NMR signal by a factor greater than 10^4 over a short period of time. Spectroscopic carbon MRI (^{13}C-MRSI), combined with DNP to hyperpolarize metabolic substrates, is a very sensitive method for real-time metabolic *in vivo* imaging and enables a non-invasive investigation of metabolic processes of living organisms.

This dissertation illustrates the establishment and application of new imaging techniques for investigating the tumor structure, as well as tumor metabolism *in vivo,* by combining methods from the fields of proton magnetic resonance imaging (MRI) and carbon magnetic resonance spectroscopic imaging (^{13}C-MRSI) in different preclinical models of PDAC. The first section of this work deals with the structural heterogeneity of murine (m)PDAC in an endogenous model, using diffusion-weighted imaging (DWI). In the second part, tumor metabolism of distinct molecular subtypes of human (h)PDAC is described by hyperpolarized magnetic resonance spectroscopy (HPMRS) with HP [1-^{13}C]pyruvate (HPMRS). The last chapter describes how MRSI with hyperpolarized [1-^{13}C]pyruvate (HPMRSI) was used in the complex endogenous model of mPDAC. Overall, this work shows the establishment of three different MRI-based methods that can be applied for non-invasive characterization of tumor heterogeneity of hPDAC and mPDAC

Kurzzusammenfassung

Angesichts der zunehmenden Inzidenz ist die Bild-basierte Klassifikation des duktalen Adenokarzinoms des Pankreas (*engl. Pancreatic ductal adenocarcinoma, PDAC)* als eine entscheidende Notwendigkeit in der PDAC Forschung herausgestellt. Eines der Kennzeichen von PDAC ist die genetische und morphologische Heterogenität, die neben anderen Faktoren die Resistenz der Behandlung und die Aggressivität dieses Krebses bestimmt. In den letzten Jahren wurden verschiedene Ansätze entwickelt, um diese Komplexität von PDAC zu verstehen und zu beschreiben, insbesondere durch molekulare und strukturelle Stratifizierung in definierte Subtypen. Heutzutage werden klassische (epitheliale) und quasi mesenchymale, oder basal-ähnliche, auch squamoid genannte, Subtypen identifiziert und mit dem Überlebensvorteil und dem besseren Ansprechen der Therapie dieser Subtypen auf FOLFIRINOX bzw. Gemcitabin / Abraxane korreliert.

Die Kernspinresonanz (NMR) basiert auf der quantenmechanischen Wechselwirkung zwischen Kernspins, Magnetfeldern und Radiowellen. Die dynamische Kernspinpolarisation (DNP) ebnete den Weg für die Durchführung von NMR in Flüssigkeiten, indem Kernspins in einen hyperpolarisierten Zustand gebracht und dadurch das messbare NMR-Signal über einen kurzen Zeitraum um einen Faktor von mehr als 10^4 verstärkt wurden. Die spektroskopische Kohlenstoff-MRT (^{13}C-MRSI) in Kombination mit DNP zur Hyperpolarisierung von Stoffwechselsubstraten ist eine sehr empfindliche Methode für die Echtzeit- Bildgebung *in vivo*, die die nicht-invasive Untersuchung von Stoffwechselprozessen lebender Organismen ermöglicht.

Die vorliegende Dissertation zeigt die Etablierung und Anwendung neuer bildgebender Verfahren zur Untersuchung der Tumorstruktur sowie des Tumormetabolismus *in vivo* durch die Kombination von Methoden aus den Bereichen Protonen-Magnetresonanztomografie (*engl. magnetic resonance imaging, MRI*) und Kohlenstoff-13C-Magnetresonanzspektroskopische Bildgebung (*engl. carbon magnetic resonance spectroscopic imaging, ^{13}C-MRSI*) in verschiedenen präklinischen PDAC-Modellen. Der erste Abschnitt dieser Arbeit befasst sich mit der strukturellen Heterogenität von murinem (m)PDAC im endogenen Modell unter Verwendung der diffusionsgewichteten Bildgebung (*engl. diffusion-weighted imaging, DWI*). Im zweiten Teil wird der Tumormetabolismus verschiedener molekularer Subtypen von menschlichem (h)PDAC durch Magnetresonanzspektroskopie mit [1-^{13}C]Pyruvat (*engl. magnetic resonance spectroscopy with HP [1-^{13}C]pyruvate, HPMRS*) beschrieben. Im letzten Kapitel wurde die chemische Shift-Bildgebung mit [1-^{13}C]Pyruvat (*engl. magnetic resonance spectroscopic imaging with hyperpolarized* [1-^{13}C]*pyruvate HPMRSI*) im komplexen endogenen Modell von mPDAC etabliert. Zusammengenommen zeigt diese Arbeit die Etablierung von drei verschiedenen MRT-basierten Methoden zur

späteren Verwendung für die nicht-invasiven Charakterisierung der Tumorheterogenität von hPDAC und mPDAC.

List of abbreviations

%	percent
^{13}C	^{13}C carbon isotope
ADC	adherent diffusion coefficient
ADEX	aberrantly differentiated endocrine exocrine
ALT	alanine aminotransferase
CA	carbohydrate antigen
DNP	dynamic nuclear spin polarization
DWI	diffusion-weighted imaging
FDG	2-Fluor-2-desoxy-D-glucose
FOV	field of view
GEMM	genetically engineered mouse models
h	human
HP	hyperpolarized
K	kidney
LDH	lactate dehydrogenase
M	murine
MRI	magnetic resonance imaging
MRS	magnetic resonance spectroscopy
MRSI	magnetic resonance spectroscopic imaging
NMR	nuclear magnetic resonance
PanIN	pancreatic intraepithelial neoplasia
PDAC	pancreatic ductal adenocarcinoma
PDX	patient-derived xenograft
PET	positron emission tomography

QM	quasi-mesenchymal
RARE	rapid acquisition with relaxation enhancement
ROI	region of interest
T	tumor
TE	echo time
TR	repetition time
TCA	tricarboxylic acid cycle
TE	echo time
TR	repetition time
T2w	T2 weighted
V	vessel

1. Introduction

1.1 Pancreatic ductal adenocarcinoma (PDAC)

Pancreatic adenocarcinoma (PDAC) is the 7th most common cancer-related cause of death worldwide and the 14th most common cancer (International Agency for Research on Cancer 2018). It is predicted to become the 2nd most common cause of cancer-related death in the western world by 2030, with prevalence and mortality anticipated to increase – especially in industrialized countries – due to a combination of nutritional risk factors (e.g. obesity, smoking, alcohol), an aging population and a lack of specific treatment options. 5-year relative survival rates of pancreatic cancer with all stages combined, remain poor at 9% (Rahib, Smith *et al.* 2014, McGuigan, Kelly *et al.* 2018, Siegel, Miller *et al.* 2020). The high mortality rate can be ascribed largely to late presentation of disease, when only 10-15% of patients are eligible for surgical resection (Hidalgo 2010) – patients found to have pancreatic cancer mostly present with non-specific symptoms, including asthenia (86%), weight loss (85%), anorexia (83%) and abdominal pain (79%). The most frequent signs are jaundice (55%) and hepatosplenomegaly (39%) (Miquel Porta 2005). Carbohydrate antigen (CA) 19-9 is the only blood-derived biomarker for PDAC – but a poor one given that it is elevated in 30%-40% of benign diseases of the pancreas (Satake, Kanazawa *et al.* 1985, Rosty and Goggins 2002) – with a sensitivity of 79% (70%-90%) and specificity of 82% (68%-91%) for PDAC (Goonetilleke and Siriwardena 2007).

Infiltrating PDAC accounts for over 90% of exocrine pancreatic cancer. This type of cancer initiates within the part of the pancreas which produces digestive enzymes, so called acini, and has a glandular epithelium (Klöppel and Lüttges 2001). The development from acini to pancreatic intraepithelial neoplasia (PanIN) lesions into PDAC is a multistep process (Figure 1) (Hidalgo 2010). PanIN lesions are subdivided into low- (PanIN-1A/1B), medium- (PanIN 2) and high- (PanIN3) grade lesions (Hruban, Goggins *et al.* 2000). At the genetic level, almost 90% of the earliest-stage, lowest-grade PanIN-1 lesions contain overactivation in the Kras oncogene, followed by loss of tumor suppressors p16/p19 (CDKN2A, 11.5%) (Kanda, Matthaei *et al.* 2012). Late lesions (PanIN-3) are associated with inactivating mutations, deletions in tumor suppressor protein p53 (TP53), breast cancer type 2 susceptibility protein

(BRCA2) and mothers against decapentaplegic homolog 4 (SMAD4) (Ferro and Falasca 2014, Weissmueller, Manchado *et al.* 2014).

For decades pathologists stratified cancers according to their histopathology, mostly due to the high costs and limited availability of molecular and genetic data.

However, contemporary researchers have developed molecular subtyping for classifications of PDAC, based on transcription and epigenetic pattern (Collisson, Bailey *et al.* 2019). Although several subtypes have been identified – such as "basal-like", "normal" or "activated" stromal subtypes (Moffitt, Marayati *et al.* 2015), as well as squamous, immunogenic or pancreatic progenitor subtypes (Bailey, Chang *et al.* 2016) – all seem derived from two more general original subtypes; Classical and the Quasi-mesenchymal (QM, squamous, basal-like) as defined by Collisson et al. in 2011 and further summarized in the latest review (Figure 2, (Collisson, Bailey *et al.* 2019)). QM subtype shows a poor survival compared to the classical subtype (Collisson, Sadanandam *et al.* 2011). This stratification is also reflected in the therapy response studies of PDAC and will be discussed in the next chapter (Collisson, Bailey *et al.* 2019).

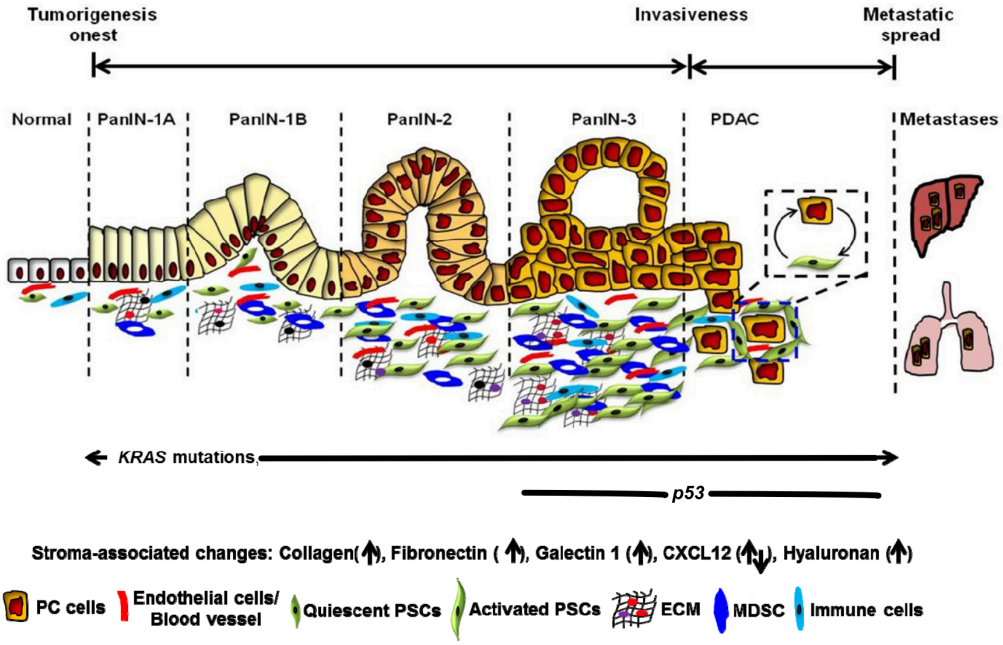

Figure 1: Simplified tumorigenesis of PDAC. Adapted from (Khan, Azim et al. 2017).

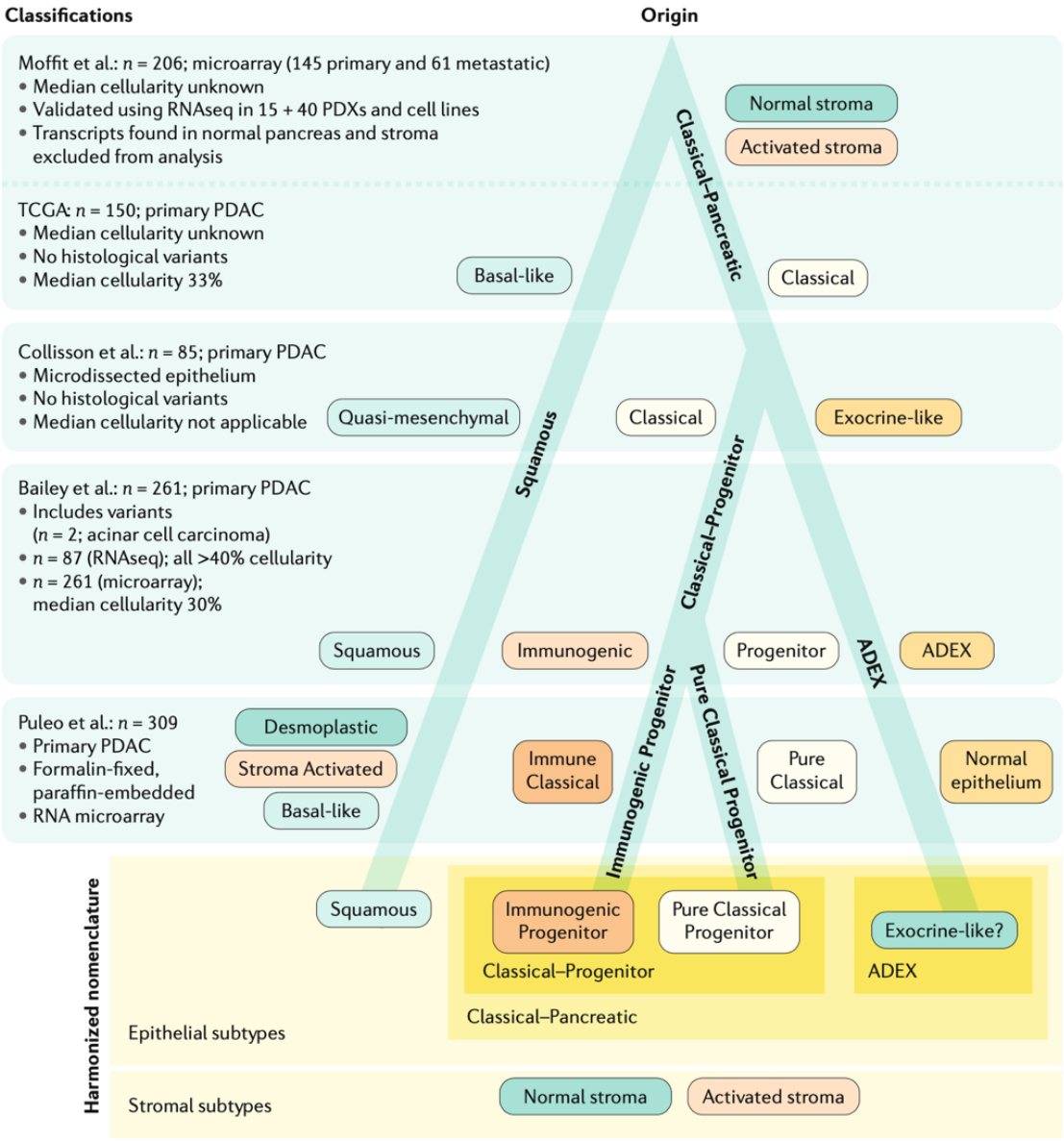

Figure 2: Phylotranscriptomic tree of pancreatic cancer in literature. Published in (Collisson, Bailey et al. 2019).

1.1.1 Therapy of PDAC

Due to the diagnostic shortcomings for PDAC, efficacious therapeutic options are very limited with little change over decades. Although the genetic events that lead to PDAC are well-known, most of these mutations are simply untreatable. Despite enormous efforts and several promising attempts to develop molecular targeted therapies for PDAC, most of the clinical trials failed within phase II. For example, specific inhibitors of MEK or PI3K signaling pathways have so far not achieved any improvement in prognosis of PDAC patients, or have been discontinued due to high toxicity (Grasso, Jansen *et al.* 2017).

In addition, therapy is complicated in this area by a tumor-induced hypovascularization, which limits the bioavailability of the active substances (Olive, Jacobetz *et al.* 2009, Provenzano, Cuevas *et al.* 2012, Jacobetz, Chan *et al.* 2013). New therapeutic approaches have been developed that aim to change the tumor microenvironment, e.g., PEGPH20, a drug that reduces internal tumor pressure, in turn making the tumor-node more accessible to chemotherapeutic agents (Jacobetz, Chan *et al.* 2013). This is based on the fact that hyaluronic acid (HA) is a major component of the extracellular matrix, such that the more of it there is, the more it should raise the interstitial gel fluid pressure within tumors and reduce drug delivery to malignant cells. This has already demonstrated promising preclinical results in first-line treatment of metastatic PDAC and early clinical evidence of efficacy, with further studies underway (Wong, Horton *et al.* 2017, Hingorani, Zheng *et al.* 2018).

As of now, the only curative option is considered to be surgery. However only 10-15% of the patients are diagnosed with a localized disease allowing a R0-surgical management (Jeune, Coriat *et al.* 2019). The majority of PDAC patients are treated according to their general condition with chemotherapy, wherein only two treatment options of chemotherapeutic substances are employed: 1) FOLFIRINOX (a combination of 5-Floururacil, folic acid, irinotecan and oxaliplatin) is used for patients with better health status (Conroy, Hammel *et al.* 2018) and 2), with albumin-conjugated Paclitaxel (Abraxane) with Gemcitabine as a palliative treatment. As described above, it has been noted that different molecular subtypes reveal distinct responses to treatment. First-line chemotherapy (FOLFIRINOX) fared significantly better in patients with the classical subtype compared to those with the QM subtype (Aung, Fischer *et al.* 2018). Another study showed that FOLFIRINOX combination chemotherapy induced a frequent shift from classical and QM PDAC to a QM state in cell lines and

patient tumors (Porter, Magnus *et al.* 2019). These data illustrate the importance of identifying PDAC subtypes and - considering plasticity of classical / QM states – the continued monitoring thereof, to fuel the development of personalized treatment regimen.

A promising new approach for treatment of many tumor entities, including PDAC, is to target tumor metabolism. In 2015 Daemen and colleagues identified that classical and QM cell lines correlate with lipogenic and glycolytic metabolic subtypes correspondingly and react differently to inhibitors (Daemen, Peterson *et al.* 2015).

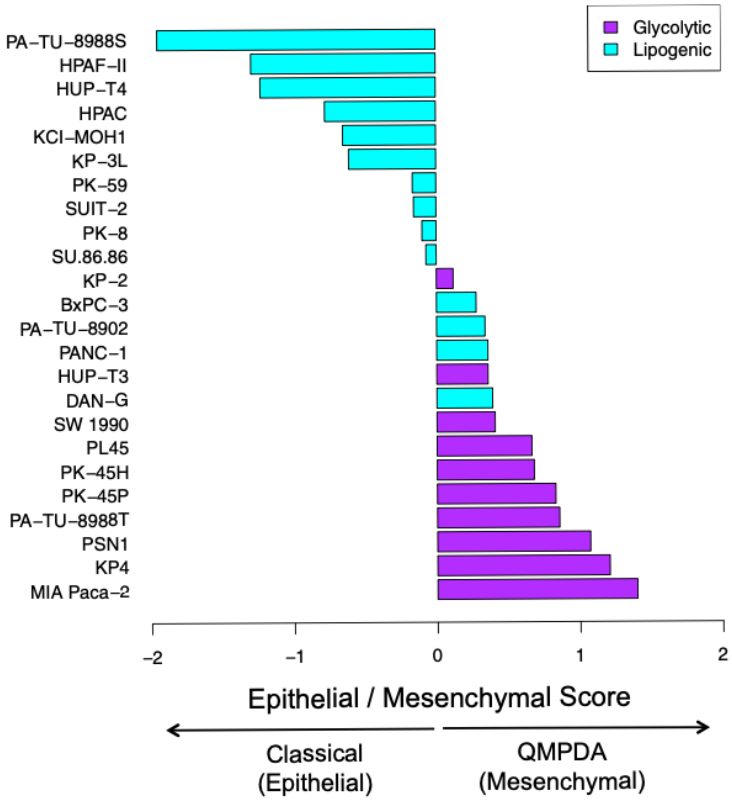

Figure 3: Subtypes of PDAC with different sensitivities to metabolic inhibitors. (Daemen, Peterson et al. 2015).

For example, both subtypes showed different metabolite levels associated with glycolysis and lipogenesis (Figure 3). Also, at transcription level, the differences in glucose and glutamine utilization, redox levels, as well as mitochondrial function, have been verified. These differences result in varying cell sensibility to inhibitors of glucose and lipid metabolism *in vitro*: e.g. the glycolytic subtype was more sensitive to Oxamate and the lipogenic subtype to a Stearoyl-CoA Desaturase (SCD) inhibitor.

Another example is CPI-613, a drug that inhibits tumor-specific energy metabolism at the cell mitochondria (Zachar, Marecek *et al.* 2011). It showed strong antitumor activity *in vivo* against human pancreatic cancers in xenograft models with low side-effect toxicity. Additionally, a phase I study in humans with metastatic PDAC was able to show low side effects when used in combination with FOLFIRINOX (Zachar, Marecek *et al.* 2011, Alistar, Morris *et al.* 2017). FX11, a small-molecule inhibitor of LDH-A was also tested in patient-derived mouse xenograft (PDX) models of PDAC (Rajeshkumar, Dutta *et al.* 2015). Pyruvate is preferentially metabolized to lactate by the enzyme lactate dehydrogenase-A (LDH-A) while aerobic glycolysis is running. Results showed that p53 status of the PDX tumor determined the response to FX11, while tumors with mutant TP53 showed attenuated tumor growth, increased apoptosis and reduced proliferation indices when exposed to FX11. The induced changes are designed to take the tumor out of its delicate balance and destroy it in combination with standard cytotoxic therapy.

1.1.2 Mouse models of PDAC

The use of animal models of PDAC is of great importance to experimental researchers – these models mimic human tumors very well and facilitate the study of malignant development in a biological context, with all the complexities of the tumor / host interactions (stromal signals, angiogenesis, inflammation, immunity, etc.) (Morton, Karim *et al.* , Clark, Hingorani *et al.* 2007, Olive, Jacobetz *et al.* 2009). Today, genetically modified mice (GEMM) are widely employed in all fields of pancreatic cancer research. The most used models are those with pancreas-specific expression of $Kras^{G12D}$ and deleted Tp53 (*Ptf1*$^{Cre/wt}$ *Kras*$^{G12D/wt}$ *P53*$^{fl/fl}$, (CKPlox))(Bardeesy, Aguirre *et al.* 2006). The simultaneous pancreatic activation of $Kras^{G12D}$ in addition to a full or partial deletion of Tp53, significantly increases the heterogeneity of pancreatic carcinomas resulting from PanIN and IPMN lesions (Khan, Azim *et al.* 2017). Normally CKPlox animals develop tumors between 6 and 14 weeks of age and succumb to the disease at approximately 70 days. These mice are very suitable for imaging, because their tumor incidence is 100%, an important feature for planning and handling. Mice with pancreas-specific expression of overactivated $Kras^{G12D}$ and deleted Tp53 ($Ptf1^{Cre/wt}$ $Kras^{G12D/wt}$ P53 $^{fl/wt}$ (CKP+-)) (Bardeesy, Aguirre *et al.* 2006), as well as animals with overexpression of the transforming growth factor -α (TGF-α) under the elastase promoter (*Ptf1*$^{Cre/wt}$ *Kras*$^{G12D/wt}$ *P53* $^{fl/wt}$ *Ela-TGFa (CKP+-T))* (Siveke,

Einwächter *et al.* 2007, Heid, Steiger *et al.* 2017), were also used to increase heterogeneity. These animal models have often been used in studies of imaging methods because they mimic human disease very well in terms of abundant fibrosis and resistance to therapy (Serrao, Kettunen *et al.* 2016, Heid, Steiger *et al.* 2017, Trajkovic-Arsic, Heid *et al.* 2017).

1.2 Imaging

Multiphasic, multi-detector computed tomography (MDCT, CT) with iodine contrast agent (CA) is recommended for PDAC patient staging (Kaissis and Braren 2019). CT provides a short one-stop-shop staging exam that usually covers thorax and abdomen / pelvis. With technical developments in recent years, multiparametric magnetic resonance imaging (mpMRI) has become a complementary tool, especially Magnetic Resonance cholangiopancreatography (MRCP) and diffusion weighted-MRI or short diffusion weighted imaging (DWI). Recent studies showed a higher sensitivity, specificity and accuracy of mpMRI for the detection of PDAC compared to CT (Toft, Hadden *et al.* 2017). However, mpMRI, and DWI in particular, not only detects PDAC but in combination with advanced image postprocessing (i.e. radiomics and machine-/deep-learning) approaches may even predict different PDAC subtypes (Kaissis, Ziegelmayer *et al.* 2019). New methods of metabolic imaging with HP substrates are currently under investigation, to add more information about different tumor types and the ensuing therapy (Hesketh and Brindle 2018).

1.2.1 Diffusion weighted imaging (DWI)

DWI represents a promising approach in characterizing tumor composition non-invasively and without contrast agents. The sequence can evaluate the motion of water molecules, which are powered by Brownian motion, in different tissues. As far back as 1965, Stejskal and Tanner described an MR experiment that could be applied to the detection and quantification of water diffusion *in vivo*. They found that the degree of water motion is proportional to the degree of signal attenuation; an approach that remains the basis of many DWI sequences in clinical use today. (Stejskal and Tanner 1965)

The sensitivity of the DWI sequence to water motion can be varied by changing the gradient amplitude, the duration of the applied gradient, and the time interval between the paired gradients. On clinical MR scanners, the diffusion sensitivity is easily varied by changing the parameter known as the “b value”, which is proportional to the three factors. When the b value is changed, it is usually the gradient amplitude, rather than the duration or time intervals between gradients, that is altered. Water molecules with a large degree of motion or a great diffusion distance (e.g., within the intravascular space) will show signal attenuation with small b values (e.g., b = 50–100 s/mm2). By

contrast, large b values (e.g., b = 1,000 s/mm2) are usually required to perceive slow-moving water molecules or small diffusion distances, because they show more gradual signal attenuation with increasing b values. Different combinations and amounts of b values are used to calculate the apparent diffusion coefficient (ADC). Tissues with a high density which are more cellular than the tissue from which they originate, like in tumors, present a high signal in the DWI and a low ADC value.

The information provided by DWI reflects changes that occur at a histological level (Neil 1997). For this reason, the process is perceived as an advantageous tool for evaluating changes in the tumor microenvironment, both before and after treatment (Koh and Collins 2007).

In a current study, we have shown that the apparent diffusion coefficient (ADC), a DWI-derived parameter, can be used to describe PDAC cellularity (Heid, Steiger *et al.* 2017). This was illustrated in both a mouse model and in human patients. Our study identified high tumor cellularity as a negative prognostic factor in PDAC survival and developed the ADC parameter for the non-invasive identification of PDAC groups. Furthermore, ADC can be used as a biomarker for early changes under therapy, e.g. 24 hours after treatment onset. A significant increase was observed in mPDAC models (Trajkovic-Arsic, Heid *et al.* 2017).

1.2.2 ^{13}C magnetic resonance spectroscopy (HPMRS) and magnetic resonance spectroscopic imaging (HPMRSI)

It is almost 70 years since Warburg proposed that glycolysis and lactic acid fermentation was the primary cause of cancer (Warburg 1956). Whilst the theory has since been disproven, abundant lactate is nonetheless phenotypically conserved across most cancer cell types, including pancreatic cancer cells. One of the promising methods for studying metabolism is magnetic resonance spectroscopy (MRS) with hyperpolarized (HP) substrates, also called hyperpolarized magnetic resonance spectroscopy (HPMRS). This technique fosters identification and quantification of metabolites in real time *in vivo*, by providing functional and quantitative rather than anatomical information, as is the case with routine MR imaging.

^{13}C magnetic resonance spectroscopic imaging (MRSI) using ^{13}C -labelled substrates, then called hyperpolarized magnetic resonance spectroscopy imaging (HPMRSI), in which the ^{13}C nuclear spins have been hyperpolarized using dynamic nuclear polarization, has revolutionized metabolic imaging with MR by increasing the sensitivity of detection >10,000-fold (Ardenkjær-Larsen, Fridlund *et al.* 2003). ^{13}C pyruvate, is the most commonly used substrate for metabolic imaging. The advantage of pyruvate is that the inserted metabolite is structurally identical to its non-labelled counterpart. Following delivery via the circulation, the molecule is rapidly transported into cells on the monocarboxylate transporters (MCTs). Unlike traditional probes, labelled metabolites can participate and inform of the modified metabolism within a cancer cell. Pyruvate is created in the cytoplasm as the endpoint of aerobic glycolysis. It can be used in tricarboxylic acid cycle (TCA), also be transaminated into alanine catalyzed by alanine aminotransferase (ALT), or under anaerobic circumstances can be transformed into lactate by lactate dehydrogenase (LDH) (Figure 4)(Brindle 2015).

Figure 4: Metabolism of Pyruvate in pancreatic cells.

Flux of hyperpolarized ^{13}C label from injected pyruvate into the endogenous lactate pool has been used to grade breast cancer, with more aggressive tumors showing more lactate exchange (Gallagher, Woitek *et al.* 2020). ^{13}C- Pyruvate MRSI can detect

early responses to drug treatment (Day, Kettunen *et al.* 2007, Ros, Wright *et al.* 2020), wherein general lactate labelling is decreased in responding tumors (Comment and Merritt 2014). Studies of treatment response were made in which hp MRI visualized the Warburg effects and predicted treatment response to mTOR inhibitors in patient-derived clear cell renal cell carcinoma (ccRCC) xenograft models (Dong, Eskandari *et al.* 2019). ^{13}C-magnetic resonance spectroscopic images of the pancreas, following injection of hyperpolarized [1-^{13}C]pyruvate, showed a decrease in the [[1-^{13}C]alanine] / [[1-^{13}C]lactate] signal ratio with disease progression, which was explained by the changes in alanine and lactate concentrations and LDH and ALT activities (Serrao, Kettunen *et al.* 2016). Metabolic imaging data has already been shown to display the immediate intracellular conversion of HP [1-^{13}C]pyruvate to lactate particularly in aggressive PDAC xenograft models (Dutta, Perez *et al.* 2019). These experiments demonstrated the potential of dynamic metabolic flux and thereof calculated parameters as biomarkers of total lactate concentration and aggressiveness of the tumor.

1.3 Objective of study

Development of molecular imaging biomarkers for non-invasive stratification of pancreatic ductal adenocarcinoma (PDAC) is a pressing clinical need, since most patients with this condition are ineligible for curative surgical treatment. Comprehensive profiling of tissue composition and metabolism in subtypes of PDAC can be crucial for the success of treatment and response monitoring of this incurable disease.

The aim of this work was to establish structural DW- and metabolic MRS-imaging for further biomarker development in different PDAC models. The first goal was to investigate structural features captured by DWI and validate them with histopathology and morphology of the tumors in a complex endogenous mPDAC model. The second focus entailed proving the principle of detection of defined metabolic subtypes, transplanted as xenograft tumors in a nude rat model of hPDAC by metabolic imaging, using HPMRS. The final goal was the establishment of HPMRSI in the complex and very heterogeneous endogenous model of mPDAC. Here we aimed to develop a method for metabolic subtype differentiation in a preclinical relevant model, with the goal of clinical translation.

2. Material and Methods

2.1 Tumor models

All experiments were performed according to the guidelines of the local Animal Use and Care Committees.

For endogenous murine PDAC tumors, genetically engineered mice were crossed according to animal care guidelines and published crossing strategies. The genotyping was performed from ear biopsy-derived DNA by polymerase chain reaction using described primers. For the experiments, we used the following transgenic and knock-in mice.

1. Mice with pancreas-specific expressed $Kras^{wt/LSLG12D}$ and deleted Tp53 ($Ptf1^{Cre/wt}$ $Kras^{G12D/wt}$ $P53^{fl/fl}$, (CKPlox))(Bardeesy, Aguirre *et al.* 2006). Normally they develop the tumor at the age of 5-6 weeks and don´t live beyond 70 days. These mice are suitable for imaging, because the incidence of developing a tumor within seven to eight weeks is 100%. This makes imaging of the mice easily plannable. Furthermore, as with human pancreatic tumors, these tumors present with strong desmoplastic reaction and immune infiltration typical for hPDAC.

2. Mice with pancreas-specific expressed $Kras^{G12D}$ and deleted Tp53 ($Ptf1^{Cre/wt}$ $Kras^{G12D/wt}$ $P53^{fl/wt}$)CKP+-(Bardeesy, Aguirre *et al.* 2006) and overexpression of the elastase promoter TGF-α (*$Ptf1^{Cre/wt}$ $Kras^{G12D/wt}$ $P53^{fl/wt}$ Ela-TGFa) CKP+-T* (Siveke, Einwächter *et al.* 2007, Heid, Steiger *et al.* 2017). The simultaneous pancreatic activation of $Kras^{G12D}$ and / or TGF-α in addition to a partial deletion of TP53, significantly increases the variety of pancreatic carcinomas resulting from PanIN and IPMN lesions. For example, TGF-α promotes the development of cystic tumors, which can also be observed in humans as IPMN-like tumors. This is significant as about 20% of human pancreatic carcinomas are caused by IPMN lesions (Khan, Azim *et al.* 2017).

N_{gesamt}= 82	Cre	Kras	Plox	TGF-α
73	+/-	+/-	Lox	-
6	+/-	+/-	+/-	tg
3	+/-	+/-	+/-	wt

Table 1 Genotypes of mice which were used in experiments

For subcutaneously implanted human PDAC, a cohort of 8 male nude rats (Crl:NIH-Foxn1^{rnu}; six to eight weeks old; Charles River, Sulzfeld, Germany) was used.

2.3 Tumor implantation

Tumor implantation was achieved by subcutaneous injection (27G cannula Sterican®, B. Braun, Meisungen) of 10^6 cells (suspended in 100 ml pure medium, without supplements) in the region of the right and left flank under isoflurane anesthesia. Tumors were allowed to grow up to 4 weeks. The growth of the subcutaneous tumors was controlled by palpation; once tumor size reached approximately 1.0cm in diameter, the animals were used for the study. The Implantation took place in a full body chamber (Induction chamber Rats, Rothacher partner, Bern).

2.4 Cell harvest

Cells were cultivated in Dulbecco's modified Eagle Medium (DMEM) containing L-glutamine (Biowest, Nuaillé, France), 10% fetal calf serum (Merck, Darmstadt, Germany), 1% sodium pyruvate (Merck, Darmstadt, Germany), 1% non-essential amino acids (GE Healthcare, Chicago, USA) and 1% penicillin and streptomycin (PAN Biotech, Aidenbach, Germany) at 37 °C with 5% CO2. The medium was aspirated, then thoroughly rinsed with 10 ml PBS. The fluid was then aspirated. After that, 3.5-4ml of trypsin and trypsinate were added for 4-10 minutes in the incubator, so that the cells were well drained. Afterwards the bottle was tapped thoroughly and 8 ml medium added (with FCS). Again, the bottle was thoroughly rinsed, and the cells resuspended (Pipette at least 5x up and down with 10x pipette). Then the cells were collected in all 5 bottles and divided into 1-2 50ml falcons. The cells were centrifuged for 4 min at 1200 rpm. The medium was aspirated and all cells (from both falcons) were taken, in total 40 ml of DMEM. Approximately 100µl was taken for counting, before further centrifuged for 4min at 1200 rpm – during which process cells were counted. Subsequently, approx. 10µl of the suspension was mixed with 10µl trypan blue and 10µl of this mixture added to the cell chamber. Finally, the 4 chambers were counted (there should be about 20-80 cells / chamber)

Formula: (Chamber1 + Chamber2 + Chamber3 + Chamber4)/2*1000*40ml = XX*10^6

Following this, the medium was carefully aspirated and the cells resuspended in the DEMEM: 10 * 10^6 / 100µl. i.e. 30 * 10^6 + 200µl. The necessary amount minus 100µl was added to the cell pellet; this was not less than 300µl.

2.5 Animal anesthesia and handling for MRI measurements

Rats:

Rats were anaesthetized by continuous gaseous infusion (Isoflurantower: Dräger, Typ: Vapor 2000; 1.5 - 2.5%; O2-flow: 2 l/min; CP-Pharma, Burgdorf, Germany) and tail vein catheterized (Becton Dickinson Company, Franklin Lakes, USA) for the injection of the hyperpolarized agent. Animals were kept with an airflow at 37°C (The37Company, Amersfoort, Netherlands) and temperature and breathing were monitored with a rectal temperature probe and pressure pad placed under the animal continuously (SA Instruments Inc., New York, USA). To protect the cornea from dehydration, an ophthalmic ointment (Bepanthen® Bayer Vital GmbH, Leverkusen) was applied.

Mice:

Mice were anesthetized by continuous gaseous infusion (Isoflurantower: Dräger, Typ: Vapor 2000; 1.5 - 2.5%; O_2-flow: 2 l/min; CP-Pharma, Burgdorf, Germany). For HPMRSI, mice were also tail vein catheterized (Becton Dickinson Company, Franklin Lakes, USA). During imaging, animals were maintained under isoflurane. Temperature and breathing were monitored continuously with a rectal temperature probe and pressure pad placed under the animal, while eyes were protected with an eye ointment (Bepanthen® Bayer Vital GmbH, Leverkusen). Animals were placed in prone position with head first in the 7T MR Scanner. Mouse breathing rate was kept at a low frequency of 30-50 min^{-1} and temperature was maintained above 37°C. Slice and field of view were positioned based on anatomical T2w coronal and axial images.

The mice were euthanized by cervical dislocation after general anesthesia was administered.

2.6 Imaging system

Experiments were performed in a 7.0 T small animal MRI scanner with a MR901 magnet (Agilent Technologies Inc., Santa Clara, USA) and Bruker AVANCE III HD

electronics (Bruker Corporation, Billerica, USA), running on Paravision software release 6.0.1. The system was equipped with Agilent Discovery HD gradient coil with an OD/ID of 305/210 mm, providing maximum gradient strength of 300 mT/m.

For endogenous mouse imaging a dual-tuned $^{13}C/^{1}H$ Tx/Rx volume resonator (RAPID Biomedical GmbH, Germany) was used with outer and inner diameters of 87 and 31 mm. Rat subcutaneous tumor imaging employed a dual-tuned $^{13}C/^{1}H$ Tx/Rx volume resonator (RAPID Biomedical GmbH, Germany) for proton imaging transmission and reception and for ^{13}C radiofrequency (RF) transmission, spectroscopy signal was received by a 20 mm ^{13}C surface coil (RAPID Biomedical GmbH, Würzburg-Rimpar, Germany). The coil could provide a maximum peak transmit power of 1 kW and had a resonator length of 46 mm and 43 mm for ^{1}H and ^{13}C imaging, respectively. For EMI-shielding, the coil had a cylindrical layer of 9µm thick copper foil and 1µm thick FR4 around its components, with no front and rear shielded caps.

2.7 Anatomic imaging

Based on mean survival time and observed approximate tumor onset time, regular anatomy screening was performed for mice by T2 weighted (T2w) MRI. Thereby, mice were subjected to serial T2w MRI scans from 6-8 weeks of age onwards. Tumors were identified by T2w RARE anatomical imaging (minimum 25 slices, echo time (TE) 90 ms, repetitions time (TR) of at least 3 s, dependent on number of slices required to cover the tumor, Matrix of 2280x 764 Pixel; 28x16 mm^2 field of view (FOV)).

2.8 DWI

The mouse bed position was adjusted until the tumor was placed in the center of the coil. DWI used a single-shot echo-planar imaging (EPI)-readout with 12 b-values (12.37 - 1528.45 s/mm^2), effective TE 34 ms, TR 5000 ms, 10 repetitions, no averaging, 9 slices, 1 mm slice thickness, receive bandwidth 100 kHz, 28x18 mm^2 FOV, voxel size 0.25x0.25x1 mm^3, partial-Fourier factor 1.6, and total scan time of 10 min. Imaging was conducted without breath gating.

ADC Fitting: Magnitude images were fit in MatLab with a least-squares model at each voxel for the apparent diffusion coefficient (ADC). To compensate for motion artifacts, which are inconsistent with normally distributed noise, fitting was iterative: First, all repetitions of all b-values were fit. A second fit excluded any repetition beyond a

threshold (the median value of the 5D image) from the initial fit at that b-value. A third fit repeated this, using the result of the second fit to determine excluded points.

Group Comparisons: Tumor ADCs were drawn within regions of interest (ROIs) on 3 adjacent slices corresponding to axial H&E tumor stainings, with the mean of the ROI-means taken as the average value for each tumor. ADCs were grouped by tumor cellularity subgroup determined from histology slices, as developed by Heid et al. 2017.

2.9 Hyperpolarization of pyruvate

The hyperpolarization process was conducted as described by Hundshammer, Braeuer *et al*. (Hundshammer, Braeuer *et al.* 2018). Briefly, 14 M [1-^{13}C]pyruvate (36.7 ± 1.9 mg) supplemented with 15 mM OX063 trityl radical and 1 mM Dotarem were polarized with a HyperSense (Oxford Instruments, Abingdon, United Kingdom) for ~30 min at 1.2 K using a microwave frequency of 94.155 GHz and 100 mW power. The sample was dissolved in a solution pressurized to 10 bar and heated to 180 °C containing 4.5 ± 0.3 mL (Scale: Kern, Typ: ABT 220 5DM) 100 mM phosphate buffered saline (PBS) (10xPBS, Biochrome), supplemented with 100 mM sodium hydroxide (NaOH) and 0.1 g/L sodium ethylenediaminetetraacetic acid (EDTA). Finally, the solution for injection contained an average pyruvate concentration of 90.3 ± 3.9 mM at pH 7.6 ± 0.2 (pH-meter: SI Analytics, Typ: ProLab4000, Electrode: pH electrode: N6000A, Weilheim, Germany). The polarization level was about 38% (measured at B0 = 1 T, Spinsolve Carbon, Magritek, Aachen, Germany) (Hundshammer, Duwel *et al.* 2018).

2.10 Magnetic resonance spectroscopy

For subcutaneous tumors, spectra were acquired with a dynamic, slice-selective spectroscopy sequence at the following parameters: 2 kHz receive bandwidth; 512 acquisition points; center frequency 175 ppm; 2 s repetition time (TR); 1.032 ms echo time (TE); 5° flip angle and a slice thickness of 10 mm. Data acquisition commenced upon dissolution and 90 spectra were acquired over 180 s. Slice positioning was based on anatomical T2w coronal and axial images (coronal: field of view 128 x 72 mm; TR 3000 ms; TE 20 ms; slice thickness 1 mm; data matrix 256 x 144; 36 slices; axial: field of view 72 x 54 mm; TR 4 s; TE 48 ms; slice thickness 2 mm; data matrix 240 x 180;

35 slices). Custom data analysis software, written in Matlab, was used for data analysis.

2.11 Chemical shift imaging

Dynamic multi frame ^{13}C spectroscopic imaging was performed with a 2D phase-encoded chemical shift imaging sequence, with temporal resolution of 5-6 s and a flip angle of 5°, TE = 1.101 ms; TR = 44.643 ms; in-plane resolution = 3x3 mm^2; number of slices = 1; slice thickness = 3 mm; averages = 1; repetitions = 42; bandwidth = 2000 Hz.

Experimental data were processed and analyzed using MatLab (R2018b) by MathWorks, Inc. (Natick, MA). Regions of interest (ROI) for tumors were drawn on T2w and copied to corresponding HPMRS-image, corrected for possible maladjustment. The area under the curve integrated over time delivered the values $AUC_{pyruvate}$ (AUC_p) and $AUC_{lactate}$ (AUC_l), as described in Hill, 2013 (Hill, Jamin *et al.* 2013).

2.12 Histology

Upon euthanization, mPDAC were removed from the abdominal cavity with surrounding organ structures (liver, spleen, gut, kidneys) to prevent change in orientation and facilitate exact correlation of imaging plane and histology based on extra-tumoral anatomical landmarks. After 48 h fixation in 4% paraformaldehyde in PBS and paraffin embedding, tumors were cut in axial slices through mouse abdomen in a series of 10 slides of 200µm distance. One slide of each series was stained with hematoxylin and eosin (H&E) staining and all available tumor bearing slides were correlated with DWI. Classification was completed as described by Heid *et al. (Heid, Steiger et al. 2017).* mPDAC were classified as high-level cellular ($PDAC^{high}$) in case of predominantly solid growth pattern with >70% tumor cells (reflecting PDAC variants such as adenosquamous or medullary carcinoma) and only very small amounts of accompanying stroma within the cluster region. Medium level cellular tumors ($PDAC^{med}$) showed a classical tubular growth pattern but exhibited clusters of small irregular glands (30–70% of tumor cells within the cluster area). Morphologically, these clusters consisted of neoplastic cells with solid cribriform or gyriform growth patterns, or otherwise with single pleomorphic tumor cells. PDAC were classified as low-level cellular ($PDAC^{low}$) if no tumor cell cluster greater than or equal 1 mm^2 was found in any

of the localizations investigated. The tumors were reviewed at least three times and the results were reproducible in all three replicates.

2.13 Genotyping

Samples came in the mix of DirectPCR (tail) buffer (Viagen cat # 102-T) 200 µl and proteinase K (Roche # 03115828001) 10µl and were then incubated > 4 hours at 55 °C. Thereafter, the proteinase was deactivated at 85 °C for 30-45 min, prior to centrifuging for 30-60 seconds at 14000 rpm. Subsequently, the supernatant was transferred to new tubes and 1 ul thereof used as template for PCR. For PCR master mix, the REDTTaq ReadyMix PCR Reacion Mix (Sigma #R252-100RXN) was used.

2.14 Statistical analysis

All statistical analyses were performed using Prism 7 (GrapPad Software). A two-sided p-value of 0.05 was chosen as cutoff value for statistical significance. ANOVA, or unpaired students t-test was performed for group comparisons of normally distributed quantities. Testing for normal distribution was conducted using Kolmogorov- Smirnov test and all groups were found to be normally distributed.

2.15 Buffers and Solutions

All chemicals used in this project were standard products purchased from Roth, Fluka, Merck and Sigma, unless specifically indicate.

3. Results

3.1 T2w for tumor detection

A high resolution axial T2w sequence was established at 7T preclinical scanner (Figure 5). The normal pancreas was rarely visible on the T2w images acquired on 7T MRI. Once pancreatic neoplasia accompanied by the inflammatory response of the nearby tissue and the resultant edema occurred, the murine pancreas was clearly visible as a hyperintense and heterogenous region between the duodenum and the spleen. T2w-MRI on 7T scanner allowed clear identification of solid pancreatic nodules in all regions of the pancreas. The tumors appeared mostly as roundish hypointense lesions compared to the adjacent preneoplastic tissue. In comparison to previous results on 1.5 T clinical scanner (Heid, Steiger *et al.* 2017), image quality and resolution was substantially improved from 0.3x0.3x0.7mm^3 voxel size (1.5T Achieva) to finally 0.13x0.13x1mm^3 voxel size. Tumors were clearly distinguished from other organs such as gut, stomach and kidney.

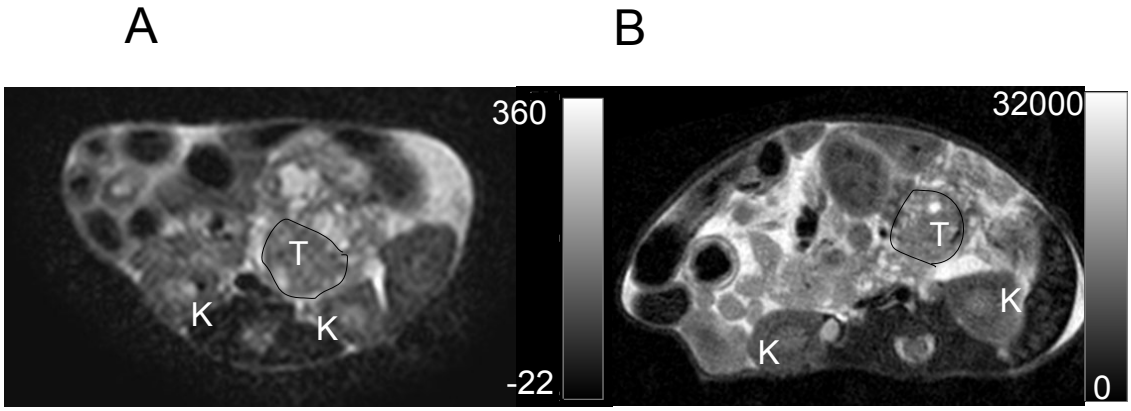

Figure 5: Comparison of anatomical imaging of mPDAC on 1.5T clinical Achieva (A) and 7T preclinical Bruker systems (B). T=tumor, K=kidney.

3.2 DWI for tumor differentiation

High resolution of DWI at 7T MRI was successfully established as free breathing method. The use of 7T scanner allowed an improvement of spatial resolution from 0.6x0.6x1.5 mm^3 voxel size (1.5T Achieva) to finally 0.25x0.25x1 mm^3 voxel size for the DWI sequence. During the process, resolutions of voxel size of 0.4x0.4x1 mm^3 and

0.25x0.25x1 mm^3 were compared (Figure 6). Higher resolution of 0.25x0.25x1 mm^3 voxel size revealed more detailed representation of the tumor composition and was deemed best suited for further experiments. PDAC subgroups (Figure 6 A-C) were divided as described in Heid *et al* (Heid, Steiger *et al.* 2017). Mean ADC values of 79 analyzed region values reliably distinguishes tumors of different cellularity ($PDAC^{low}$ 1.58±0.08; $PDAC^{med}$ 1.35±0.07; $PDAC^{high}$ 1.17 ± 0.11; All tumors included; P<0.0001 for all group comparisons. This observation was true for analysis of several tumors per mouse, as well as by choosing only one tumor for each animal ($PDAC^{low}$ 1.56±0.08, n= 8; $PDAC^{med}$ 1.32±0.09 n= 19; $PDAC^{high}$ 1.19 ± 0.08 n= 9) P<0.0001 for all group comparisons (Figure 7 D, E).

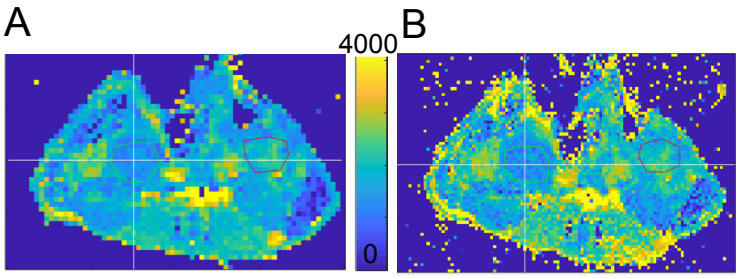

Figure 6: Different resolutions of an ADC map 0.4x0.4x1mm^3 (A) vs. 0.25x0.25x1mm^3 (B). The ROI indicates the location of the solid tumor nodule.

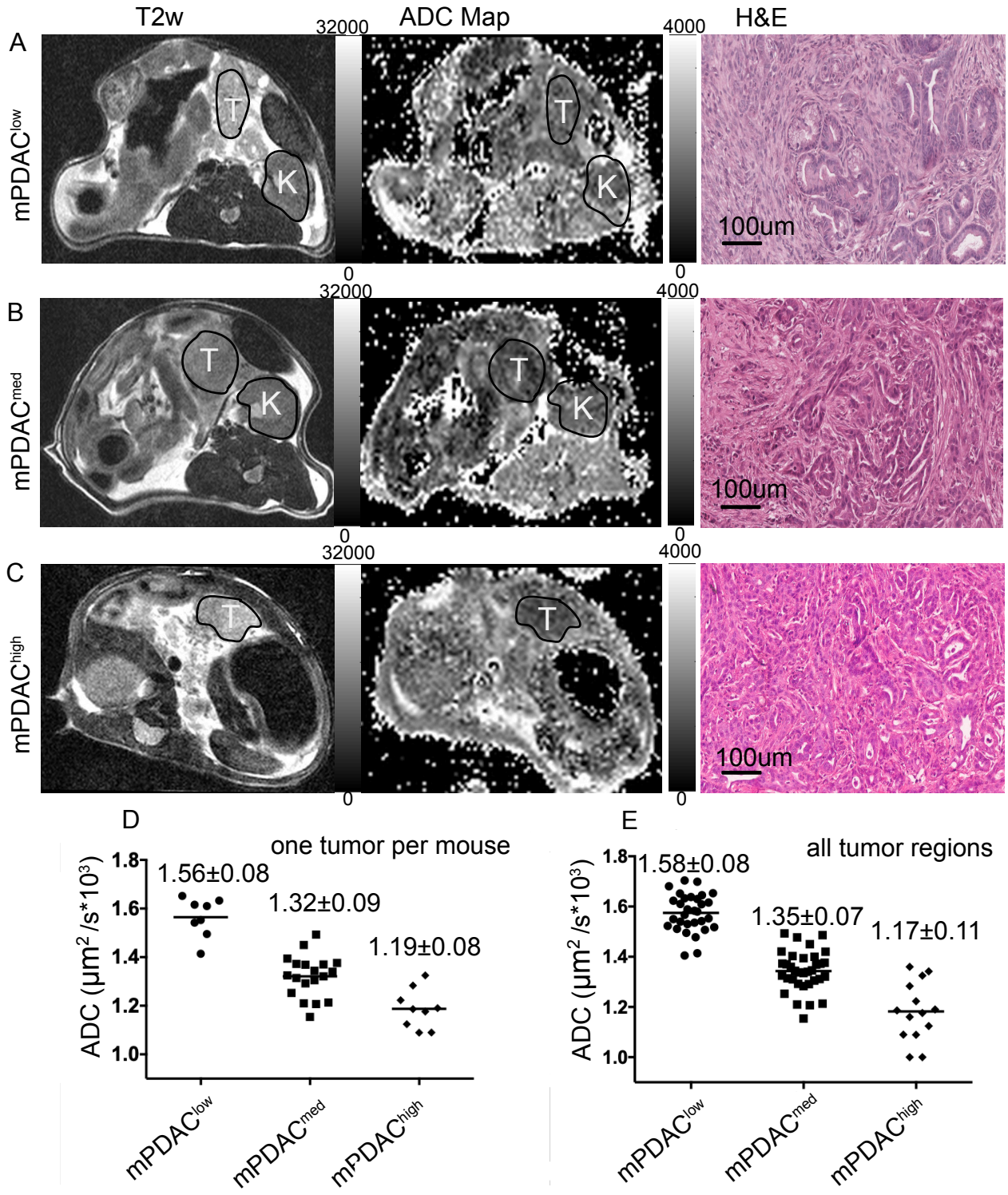

Figure 7: DWI reliable distinguish murine PDAC tumors by tumor cellularity. Slice-based correlation of imaging and histology with tumor (T) and kidney (K). T2w image, ADC map, and corresponding magnified tumor histopathology.

- *A) T2w, ADCmap and histology of mouse with PDAC^{high} tumor region (ADCmean = 1.154µm^2/s*10^{-3})*
- *B) T2w, ADCmap and histology of mouse with PDAC^{med} tumor region (ADCmean = 1.259µm^2/s*10^{-3})*
- *C) T2w, ADCmap and histology of mouse with PDAC^{low} tumor region (ADCmean = 1.652µm^2/s*10^{-3})*

D) Subgroup differentiation with ADC mean values. Presented is one tumor region per mouse. Mean values and standard deviation are given above each group.

E) Subgroup differentiation with ADC mean values. Presented are all tumor regions, that could be correlated, also multiple tumor regions per mouse. Mean values and standard deviation are given above each group.

3.3 PDAC subtype differentiation in xenografts in a nude rat model using HPMRS with [1-^{13}C]pyruvate

In order to test differences in tumor metabolism for non-invasive subtype differentiation in PDAC, HPMRSI with [1-^{13}C]pyruvate was applied in a subcutaneous (s.c.) nude rat model of hPDAC. Here fore, eight well characterized and described as metabolically different, established human cell lines (Daemen, Peterson *et al.* 2015) were transplanted into the flank of the nude rats. Of the eight transplanted cell lines, five grew in the s.c. nude rat model; three classical (HPAFII, HPAC, PaTU-8988S) and two QM (MiaPaca2, PSN1). Histological analysis of grown tumors revealed typical histology for epithelial tumors of the classical cell lines (Figure 8A), with tumor cell clusters and ductal structures surrounded by prominent stroma. In contrast, QM tumors show rather large areas of cell clusters, with stromal branches only rarely present. Tumors were clearly visible on axial T2w-images (Figure 8B) and ranged between 10mm and 15mm in diameter. Functional metabolic measurements of HPMRS were established and worked reliably in this models. Signal to background ratios of pyruvate signal were 9±2, and lactate 4±2 (Figure 8C). Even though the pyruvate signal of the cell lines was almost equally high, suggesting no differences in the delivery to the tumors, the lactate signal of the C cell lines was clearly lower than the signal in the QM cell lines (Figure 8C). Figure 8D shows an example of the distribution of signal intensity over time, revealing similar pyruvate signal and lower lactate production signal in C compared to QM cell lines. Repeated measurements with the same cell lines in different rats produced similar findings, showing stability of the model and measurement (Figure 8E, F). Finally, QM cells showed higher lactate to pyruvate conversion ratios (AUC_l/AUC_p=1.510 ± 0.16) compared to tumors of C lines (AUC_l/AUC_p = 0.7467 ± 0.12) $P<0.0001$, functionally confirming higher glycolytic turnover in the QM compared to C PDAC *in vivo* (Figure 8F).

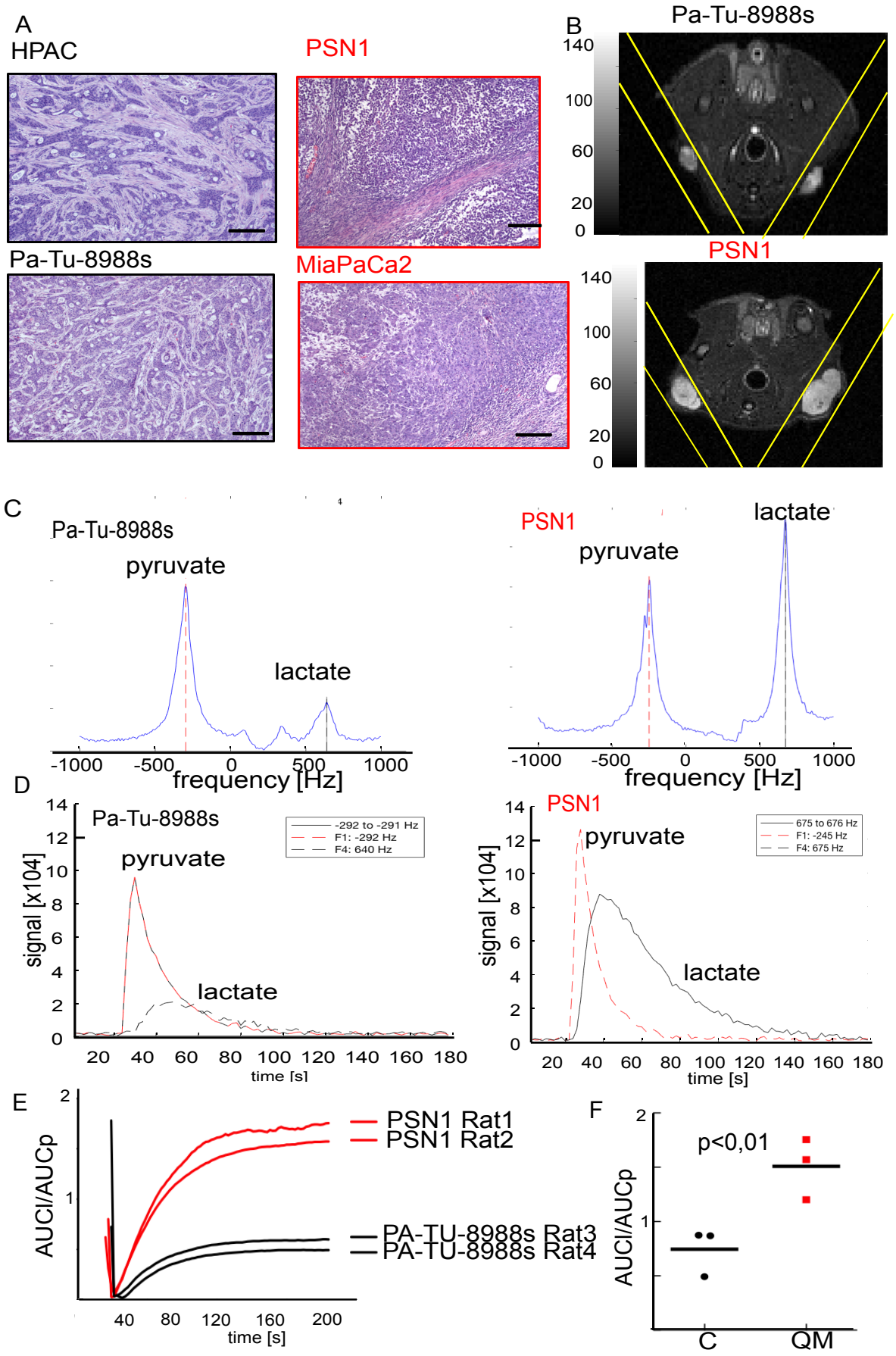
A
HPAC
PSN1
Pa-Tu-8988s
MiaPaCa2
B
Pa-Tu-8988s
PSN1
C
Pa-Tu-8988s
pyruvate
lactate
frequency [Hz]
PSN1
pyruvate
lactate
frequency [Hz]
D
Pa-Tu-8988s
pyruvate
lactate
signal [x104]
time [s]
PSN1
pyruvate
lactate
signal [x104]
time [s]
E
AUCl/AUCp
PSN1 Rat1
PSN1 Rat2
PA-TU-8988s Rat3
PA-TU-8988s Rat4
time [s]
F
AUCl/AUCp
p<0,01
C
QM

Figure 8: HPMRS detects metabolic status of different tumor subtypes in rat model of transplanted PDAC.

A) Histopathology of human s.c. tumors xenografts established in the nude rat model. Representative H&E staining of two epithelial/classical (HPAC and Pa- Tu-8988S) and two quasi-mesenchymal (PSN1 and MIaPaCa2) tumors. Scale bar 50µm.

B) T2w-MRI axial slice of the rat with two xenografts implanted. Yellow lines represent the slice orientation of the data acquisition.

C) Signal intensity of lactate and pyruvate spectral peaks from the MRS measurements of indicated tumor. The PSN1 tumor shows higher lactate peak than the Pa-Tu-8988s tumor.

D) Representative examples of pyruvate and lactate conversion over time measured via MRS in PSN1 and Pa-Tu-8988s tumors. The conversion in the PSN1 tumor is higher than in the Pa-Tu-8988s.

E) Representative example of repeated transplantation and measurements with same cell lines PSN1 and PA-TU-8988s. Presented are cumulative sums of AUC_l/ AUC_p ratios over time. The conversion of HP [1-^{13}C]pyruvate to [1-^{13}C]lactate is in the PSN1 tumors higher in both instances.

F) QM tumors (PSN1, MiaPaCa2) in two mice show higher L/P conversion rates than C tumors (HPAC,Pa-Tu-8988s). The values are shown from 3 tumors of 2 animals in each group.

3.4 HPMRSI- I*n vivo* imaging of HP [1-^{13}C]pyruvate to [1-^{13}C]lactate conversion

In order to investigate differences in glycolysis between the different tumors in the complex endogenous mPDAC model, a single slice multiframe chemical shift imaging (CSI) was successfully established on a 7T scanner. As illustrated in Figures 9A and 9B, inflow of HP [1-^{13}C]pyruvate through the vessel, as well as conversion to HP [1-^{13}C]lactate in the kidney (K) and tumor (T), were clearly visible on the calculated HPMRSI maps. The ^{13}C magnitude spectra acquired *in vivo* (Figures 9C and 9D) revealed clearly distinguishable peaks of HP [1- ^{13}C]pyruvate and HP[1-^{13}C]lactate, with signal to background ratios of >7 for pyruvate and >2 for lactate. Occasionally, HP alanine was also visible in the tumor (Figure 9D). Representative examples of the time courses of the [1-^{13}C]lactate and [1- ^{13}C]pyruvate spectral peak amplitudes, starting before and continuing during and after the injection are shown in Figures 9E and 9F. Moreover, AUC_l/AUC_p was calculated for each tumor; a $PDAC^{low}$ tumor in mouse A (Figure 9A) AUC_l/AUC_p = 0.602 and a $PDAC^{high}$ tumor in mouse B (Figure 9B) AUC_l/AUC_p = 1.470 revealed measurable differences between different tumor types.

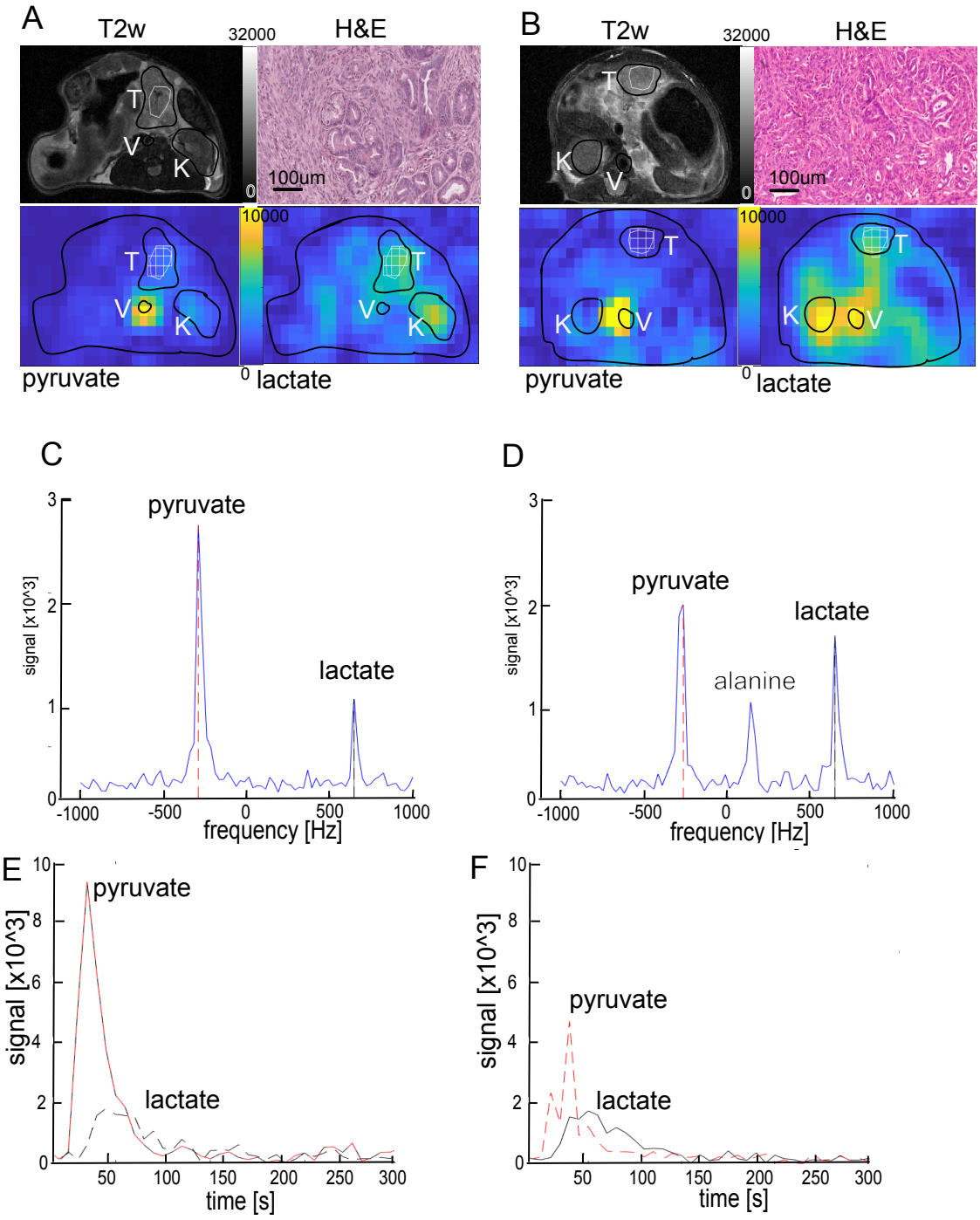

Figure 9: HPMRSI in murine PDAC

- *A) T2w MRI, histology H&E staining, [1-^{13}C]pyruvate and [1-^{13}C]lactate image at signal peak with ROI covering the tumor (T), the kidney (K) and a vessel (V) of mouse A*
- *B) T2w MRI, histology H&E staining, [1-^{13}C]pyruvate and [1-^{13}C]lactate image at signal peak with ROI covering the tumor (T), the kidney (K) and a vessel (V) of mouse B.*
- *C) Magnitude spectrum of [1-^{13}C]pyruvate and [1-^{13}C]lactate peak measured from mouse A summed over 5 frames (25s) covering the [1-^{13}C]pyruvate peak.*
- *D) Magnitude spectrum of [1-^{13}C]pyruvate and [1-^{13}C]lactate peak measured from mouse B summed over 5 frames (25s) covering the [1-^{13}C]pyruvate peak. Mouse B had also alanine measured.*
- *E) and F) Time course of the [1-^{13}C]pyruvate and [1-^{13}C]lactate spectral peak amplitudes, starting before and continuing during and after the injection in tumor region of mouse A (E) and in tumor region of mouse B (F).*

3.5 Testing of multislice chemical shift imaging for simultaneous measurement of multifocal PDAC

To properly analyze multiple tumors within one animal, a multislice (two slices) HPMRSI sequence was developed. [1-^{13}C]pyruvate was visible in the vessels and in the tumor region (Fig 9 A,B). After a few seconds [1-^{13}C]lactate peaked up and the tumor and other lactate producing organs were visible in Figures 9A and 9B. The ^{13}C-magnitude spectra acquired *in vivo* (Figures 9C and 9D) revealed clearly distinguishable peaks of pyruvate and lactate, with signal to background ratios of >8 for pyruvate and >2 for lactate (Figure 9C). A trend towards higher values was observed in PDAC^{high} tumor with higher AUC_l/AUC_p ratios than in the PDAC^{low} tumor (Figure 9D). Tumor A AUC_l/AUC_p = 0.625, tumor B AUC_l/AUC_p = 0.386.

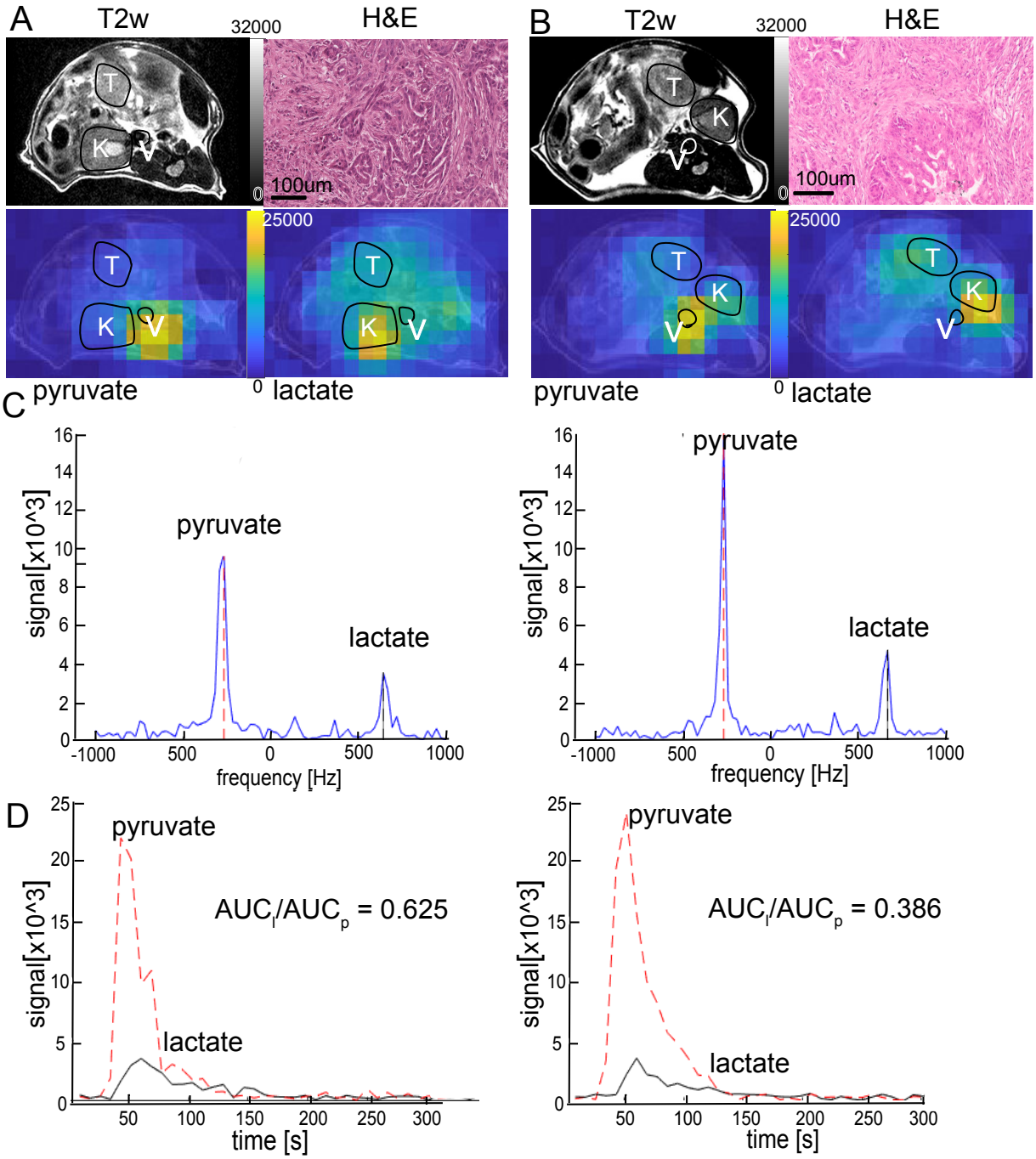

Figure 10: Multislice HPMRSI in murine PDAC

- *A) and B) T2w MRI, histology H&E staining, [1-^{13}C]pyruvate and [1-^{13}C]lactate image at signal peak with ROI covering the tumor (T), the kidney (K) and a vessel (V) of a mouse bearing 2 tumors A (mPDAC^{high}) and B(mPDAC^{low}).*
- *C) Magnitude spectrum of [1-^{13}C]pyruvate and [1-^{13}C]lactate peak measured from tumor A and B summed over 5 frames (30 s) covering the [1-^{13}C]pyruvate peak.*
- *D) Time course of the [1-^{13}C]lactate and [1-^{13}C]pyruvate spectral peak amplitudes, starting before and continuing during and after the injection in tumor region A (left) and tumor region B (right).*

4. Discussion

The development of non-invasive imaging biomarkers is an urgent need in clinical radiology. The goal of this study was to establish structural and metabolic imaging at a 7T preclinical MRI scanner, in order to visualize and quantify distinct features of murine and human PDAC in preclinical models. Here, we established T2w anatomical and DWI sequence in 7T MRI, with substantially improved resolution for better tumor delineation and analysis. In addition, the b-values amount was increased, which is necessary for further wide-ranging evaluation of DWI. We established a HPMRS sequence in two rat models of hPDAC with defined transcriptional and metabolic subtype. Moreover, HPMRSI was established in a complex mouse model of mPDAC. These methods represent important tools for future comprehensive studies of functional PDAC heterogeneity, subtyping and preclinical therapy trials.

4.1 DWI

DWI detects differences in tumor cellularity in murine and human PDAC, as demonstrated at 1.5T MRI (Heid, Steiger *et al.* 2017). Our study shows similar findings using 7T MRI. Tumor cellularity groups as defined by Heid *et al.* 2017 were clearly distinguished by the 7T MRI and revealed significant differences in mean tumor ADC values. This observation is useful for future preclinical therapy trials since increased cellularity has been linked to worsened overall survival in hPDAC (Heid, Steiger *et al.* 2017, Trajkovic-Arsic, Heid *et al.* 2017, Kaissis, Ziegelmayer *et al.* 2019). Additionally, different cellularity is linked to better/worse penetration of given therapy into the tumor (Torphy, Wang *et al.* 2018) influencing thereby therapy outcome.

Another recent study suggested, that the presence or absence of glands in histological tissue samples of PDAC patients is associated with molecular C and QM subtypes of PDAC respectively (Kalimuthu, Wilson *et al.* 2020). DWI is capable of detecting gland-forming patterns due to the higher diffusion of water molecules in glands and ducts compared to the non-glandular tissue. In mPDAC, glands and ducts are mostly present in the $mPDAC^{low}$ subgroup that is clearly distinguishable from more cellular $mPDAC^{med}$ and $mPDAC^{high}$ by high mean ADC values (Heid, Steiger *et al.* 2017). These observations are also true for hPDAC (Heid, Steiger *et al.* 2017). However, no

histological or immunohistological stainings exist for molecular subgroup identification of mPDAC, as e.g. KRT81 (QM Subtype) in hPDAC (Muckenhuber, Berger *et al.* 2018). As such, reliable differentiation of molecular subgroups with the aid of glandular pattern detected by DWI remains under investigation. Albeit, there is evidence that radiomics aproaches using DWI may represent a promising method for further discrimination of the molecular subtypes, with high sensitivity and specificity between two groups of histomorphologically defined molecular subtypes of PDAC (Kaissis, Ziegelmayer *et al.* 2019).

Mouse models mimic well hPDAC and allow us to examine parameters that require long scan times in the clinical routine and therefore not possible to investigate. For example, measuring high b-values is a rarely used clinical practice because it is highly time consuming and not suitable for every patient (Jendoubi, Wagner *et al.* 2019). We have established a DWI sequence with several high b-values (up to 1500 s/mm^2), to analyze the influence of high b-values for the detection of different subtypes in PDAC in future studies. The inclusion of DWI with b-values above 1000 s/mm^2 substantially improves the qualitative appearance of uniform region fit of ADC at 7T. This finding is in line with published studies showing that higher b-values improve tumor delineation (Ichikawa, Erturk *et al.* 2007, Fukukura, Shindo *et al.* 2016). Furthermore, ADC value calculation using high b-values might result in substantial benefits of mapping cellularity and will be investigated in subsequent studies.

In summary, DWI appears as a highly applicable tool at 7T preclinical scanner and ADC is a potential imaging biomarker for differentiation between tumor subtypes based on cellularity and morphology. Additionally, DWI reveals new opportunities in therapy monitoring given the high sensitivity of changes in cell viability (Trajkovic-Arsic, Heid *et al.* 2017). Therefore, in this work established sequences will be used as non-invasive tumor cellularity monitoring method in future planned preclinical therapy studies.

4.2 HPMRSI

Thanks to the innovation of Ardenkjær-Larsen et al. 2003, we can use different substrate and solutions for hyperpolarization, which affords us a wide variety of possibilities to show metabolic processes (Ardenkjær-Larsen, Fridlund *et al.* 2003). To date, HP[1-^{13}C]pyruvate is the most commonly used substrate for tumor detection

studies, since LDH-A expression – the main enzyme for pyruvate conversion – is significantly elevated in pancreatic and other cancers compared with normal pancreatic tissue (Rong, Wu *et al.* 2013). Albers and Bok et al. showed in 2008 that more aggressive tumors revealed increased lactate labelling in HPMRSI after [1-^{13}C]pyruvate injection (Albers, Bok *et al.* 2008). Similar results were obtained recently in breast cancer (Gallagher, Woitek *et al.* 2020) and propose a possible correlation between aggressive PDAC subtype and high glycolytic metabolism that merits further investigation.

In this study we established a reliable HPMRSI sequence for measuring HP [1-^{13}C]pyruvate and HP [1-^{13}C]lactate in an endogenous mPDAC model. In 2016, Serrao et al. published a similar study in a KPC model and showed differences between mPDAC and preneoplastic lesions in the pancreas; however, no differences between sarcomatoid tumors and mPDAC were observed (Serrao, Kettunen *et al.* 2016). Others showed differences between different tumor gradings and AUC_l/ AUC_p signal in mouse models of a prostate cancer model (Chen, Larson *et al.* 2017). Here, we have detected exemplary differences between mPDAC^{low} and mPDAC^{high} between different animals and within one animal. However, we have not yet observed any sarcomatoid tumors in our cohort, most probably due to small sample size, and therefore could not investigate this issue. In addition, all three studies reveal differences in the sequence composition and technical setup, as well as reliably detected metabolites. Thus, Serrao et al. regularly detected [1-^{13}C]alanine, in contrast to our study. Further studies involving higher subject numbers with this established sequence are necessary in order to prove usefulness of HPMRSI as biomarker for PDAC.

Pancreatic cancer is a very heterogeneous disease. Our endogeneous mPDAC models reveal high intra- and intertumoral heterogeneity and are therefore very suitable for preclinical imaging studies (Heid, Steiger *et al.* 2017). The multislice HPMRSI as applied was established as a solution for multicentric tumors. This new method makes it possible to measure at least two tumor regions in a single scan and detect exemplary differences in the metabolism of distinct tumor groups within one animal. The advantage of this method is the single injection of [1-^{13}C]pyruvate, which is far more time and cost effective than multiple injections, also reducing the burden on the animals. However, measuring two slices means reduced temporal resolution (from 5 to 6,5s), which is crucial for quick processes as metabolism. This must be

weighed against the time and cost effectiveness in further studies. Overall, a three dimensional acquisition sequence, such as bSSFP (Topping, Hundshammer *et al.* 2020) would be more helpful in measuring tumor heterogeneity and should be implemented in future studies.

Taken together, HPMRSI is a very promising new method for metabolic tumor stratification in PDAC. It must however be compared with the clinically established method of measuring metabolism – the positron emission tomography (PET) with 18F-Fluordesoxyglucose (FDG). PET Studies of FDG uptake and the overall survival in patients with pancreatic adenocarcinoma showed a strong negative correlation between these two factors (Chirindel, Alluri *et al.* 2015). HPMRSI has the advantages compared to PET measurements, since it does not require radiation and long uptake time prior the measurement, as well as detects a dynamic enzyme conversion process compared to simple glucose uptake measured by PDG-PET. However, HPMRSI is at the moment still more expensive and still requires a great deal of technical improvement before regular use in the clinical routine.

4.3 PDAC subtype differentiation in a human xenografts nude rat model

Daemen, Petersen *et al.* showed 2015 a link between classical (epithelial) and mesenchymal subtype of hPDAC and tumor metabolism in established cell lines (Daemen, Peterson *et al.* 2015). In our study we compared non-invasive metabolic imaging of epithelial with mesenchymal tumors derived from those characterized cell lines in a rat s.c. model of hPDAC and observed higher pyruvate turnover in glycolytic compared to lipogenic tumors. Thus, we detect metabolic differences in epithelial and mesenchymal tumors, a functional property that can be potentially used as a biomarker for subtyping and evaluation of the aggressiveness of PDAC. Our in vivo data correlate with previously described in vitro experiments, where increased expression of MCT4, one of the major transporters of lactate and pyruvate into a PDAC cell, has already been linked with the QM subtype of PDAC in the PSN1 cell line (Baek, Tse *et al.* 2014). Similarly metabolic imaging data of patient-derived xenografts (PDXs) showed increased intracellular conversion of HP [1-^{13}C]pyruvate to [1-^{13}C]lactate in more aggressive subtype of PDX (Dutta, Perez *et al.* 2019). Furthermore, blocking key enzymes of the tumor metabolism could be the vanguard of significantly better therapy outcomes in the future. FX11, an inhibitor of LDH-A, was shown to reduce tumor growth in PDX models of hPDAC (Rajeshkumar, Dutta *et al.* 2015). In our study,

therapy response monitoring was not investigated yet. However, HPMRS together in PDX models as well as s.c. tumor implantation model established in this study, represent excellent combinations for interrogating the efficacy of such therapies in future preclinical trials.

4.6 Limitations

The use of preclinical models for investigation of various questions is essential in imaging research and often unavoidable, due to the limitations of clinical trials. However, also preclinical models and imaging modalities suffer from following limitations.

The endogenous mouse model is repeatedly proven to faithfully recapitulate hPDAC. Ultimately, it is still a mouse model. Unquestionably, there are differences that cannot be ignored when transferring research results to humans, e.g. differences in stroma composition, ex vivo determined tissue biomarkers and possible transcriptional profiles. Furthermore, in our studies we worked with small sample sizes. The measured values cannot be referenced to normal tissue because of small size of the animals and limited spatial resolution in imaging we use. This prevents the data from being standardized. To overcome this limitation, we used only ratios of pyruvate to lactate conversion, a calculation that accounts for systemic effects and allows a comparison between the groups.

One of the major limitations of hPDAC rat model established here, is the use of cultured cells established for years. These cell lines do not represent the actual variety of PDAC cell subtypes and limit the direct translation into the clinical studies. In addition, s.c. tumors grow without any influence from the adaptive immune system, i.e. without the influence of T-cells, since an immune compromised animal needed to be used for tumors to engraft. Nevertheless, stroma is present, as can be seen in Figure 8 and thus it is relatively similar to human PDAC. Further, the s.c. implanted tumors certainly differ in their perfusion pattern compared to the endogenously grown PDAC. However, our results represent an important proof of principal experiment, that reveals the general potential of using HPMRSI for metabolic subtype stratification of PDAC.

Other limitations of HPMRSI studies with [1-^{13}C]pyruvate are high costs and required efforts. The substrate is expensive and also the technology to run the experiments.

Many highly sensitive devices are involved in the manufacture of hyperpolarized pyruvate. MRI is also an energy-intensive and vulnerable technology. To make the experiments, and the equipment used for them, leaner would greatly simplify the implementation of the experiments. Furthermore, the short half-life of the polarization of the substrate *in vivo* limits possible studies to relatively fast metabolic actions in pre-defined body regions. Although pyruvate is a naturally existing metabolite in the human and rodent body, the amount required for a sufficiently high signal for MRS or MRSI is in the hyper-physiological range. Still, no toxic effects due to pyruvate applications are known thus far (Brindle 2015) and were not observed in our study. In addition, it appears to be a powerful cardioprotective agent against the effects of myocardial ischemia-reperfusion and oxidative stress (Mallet, Olivencia-Yurvati *et al.* 2018).

Several biological, tumor specific limitations of HPMRSI with pyruvate also need to be further investigated. Delivery of the HP agent trough MCT transporters into the tumor and MRI signal dependency on it is a major point of investigation. E.g. a change in the expression or inhibition of MCTs has a great influence on the lactate formation rate measured in the HPMRS (Lodi, Woods *et al.* 2013). The conversion of pyruvate to lactate is dependent on the presence of the cofactor NADH required for this reaction, as well as the size of the endogenous lactate pool (Day, Kettunen *et al.* 2007). Finally, it must be acknowledged that the conversion of pyruvate into metabolites other than lactate was not considered here but does of course take place *in vivo*.

Conclusion

The multiparametric imaging approach applied in this study provides valuable information on tumor structure and metabolism *in vivo*. Here, we established DWI as a reliable method for the classification of tumors based on tumor cellularity parameter in a complex PDAC mouse model at a preclinical 7T MRI scanner. We also established HPMRS(I) with [1-^{13}C]pyruvate at 7T. The results on the *in vivo* detection and characterization of tumor metabolism confirm its complexity and require further investigation before general statements about tumor classification detected by HPMRSI can be made. The established work flows and methods are expected to contribute towards a successful clinical translation for HPMRSI. Especially the combination of DWI and HPMRSI may enable a more accurate prediction of PDAC subtypes.

List of Figures

List of Tables

Literature

Albers, M. J., R. Bok, A. P. Chen, C. H. Cunningham, M. L. Zierhut, V. Y. Zhang, S. J. Kohler, J. Tropp, R. E. Hurd, Y.-F. Yen, S. J. Nelson, D. B. Vigneron and J. Kurhanewicz (2008). "Hyperpolarized ¹³C Lactate, Pyruvate, and Alanine: Noninvasive Biomarkers for Prostate Cancer Detection and Grading." Cancer Research **68**(20): 8607-8615.

Alistar, A., B. B. Morris, R. Desnoyer, H. D. Klepin, K. Hosseinzadeh, C. Clark, A. Cameron, J. Leyendecker, R. D'Agostino, Jr., U. Topaloglu, L. W. Boteju, A. R. Boteju, R. Shorr, Z. Zachar, P. M. Bingham, T. Ahmed, S. Crane, R. Shah, J. J. Migliano, T. S. Pardee, L. Miller, G. Hawkins, G. Jin, W. Zhang and B. Pasche (2017). "Safety and tolerability of the first-in-class agent CPI-613 in combination with modified FOLFIRINOX in patients with metastatic pancreatic cancer: a single-centre, open-label, dose-escalation, phase 1 trial." The Lancet Oncology **18**(6): 770-778.

Ardenkjær-Larsen, J. H., B. Fridlund, A. Gram, G. Hansson, L. Hansson, M. H. Lerche, R. Servin, M. Thaning and K. Golman (2003). "Increase in signal-to-noise ratio of > 10,000 times in liquid-state NMR." Proceedings of the National Academy of Sciences **100**(18): 10158-10163.

Aung, K. L., S. E. Fischer, R. E. Denroche, G. H. Jang, A. Dodd, S. Creighton, B. Southwood, S. B. Liang, D. Chadwick, A. Zhang, G. M. O'Kane, H. Albaba, S. Moura, R. C. Grant, J. K. Miller, F. Mbabaali, D. Pasternack, I. M. Lungu, J. M. S. Bartlett, S. Ghai, M. Lemire, S. Holter, A. A. Connor, R. A. Moffitt, J. J. Yeh, L. Timms, P. M. Krzyzanowski, N. Dhani, D. Hedley, F. Notta, J. M. Wilson, M. J. Moore, S. Gallinger and J. J. Knox (2018). "Genomics-Driven Precision Medicine for Advanced Pancreatic Cancer: Early Results from the COMPASS Trial." Clin Cancer Res **24**(6): 1344-1354.

Baek, G., Y. F. Tse, Z. Hu, D. Cox, N. Buboltz, P. McCue, C. J. Yeo, M. A. White, R. J. DeBerardinis, E. S. Knudsen and A. K. Witkiewicz (2014). "MCT4 defines a glycolytic subtype of pancreatic cancer with poor prognosis and unique metabolic dependencies." Cell Rep **9**(6): 2233-2249.

Bailey, P., D. K. Chang, K. Nones, A. L. Johns, A. M. Patch, M. C. Gingras, D. K. Miller, A. N. Christ, T. J. Bruxner, M. C. Quinn, C. Nourse, L. C. Murtaugh, I. Harliwong, S. Idrisoglu, S. Manning, E. Nourbakhsh, S. Wani, L. Fink, O. Holmes, V. Chin, M. J. Anderson, S. Kazakoff,

C. Leonard, F. Newell, N. Waddell, S. Wood, Q. Xu, P. J. Wilson, N. Cloonan, K. S. Kassahn, D. Taylor, K. Quek, A. Robertson, L. Pantano, L. Mincarelli, L. N. Sanchez, L. Evers, J. Wu, M. Pinese, M. J. Cowley, M. D. Jones, E. K. Colvin, A. M. Nagrial, E. S. Humphrey, L. A. Chantrill, A. Mawson, J. Humphris, A. Chou, M. Pajic, C. J. Scarlett, A. V. Pinho, M. Giry-Laterriere, I. Rooman, J. S. Samra, J. G. Kench, J. A. Lovell, N. D. Merrett, C. W. Toon, K. Epari, N. Q. Nguyen, A. Barbour, N. Zeps, K. Moran-Jones, N. B. Jamieson, J. S. Graham, F. Duthie, K. Oien, J. Hair, R. Grutzmann, A. Maitra, C. A. Iacobuzio-Donahue, C. L. Wolfgang, R. A. Morgan, R. T. Lawlor, V. Corbo, C. Bassi, B. Rusev, P. Capelli, R. Salvia, G. Tortora, D. Mukhopadhyay, G. M. Petersen, I. Australian Pancreatic Cancer Genome, D. M. Munzy, W. E. Fisher, S. A. Karim, J. R. Eshleman, R. H. Hruban, C. Pilarsky, J. P. Morton, O. J. Sansom, A. Scarpa, E. A. Musgrove, U. M. Bailey, O. Hofmann, R. L. Sutherland, D. A. Wheeler, A. J. Gill, R. A. Gibbs, J. V. Pearson, N. Waddell, A. V. Biankin and S. M. Grimmond (2016). "Genomic analyses identify molecular subtypes of pancreatic cancer." Nature **531**(7592): 47-52.

Bardeesy, N., A. J. Aguirre, G. C. Chu, K.-h. Cheng, L. V. Lopez, A. F. Hezel, B. Feng, C. Brennan, R. Weissleder, U. Mahmood, D. Hanahan, M. S. Redston, L. Chin and R. A. DePinho (2006). "Both p16Ink4a and the p19Arf-p53 pathway constrain progression of pancreatic adenocarcinoma in the mouse." Proceedings of the National Academy of Sciences **103**(15): 5947-5952.

Brindle, K. M. (2015). "Imaging metabolism with hyperpolarized (13)C-labeled cell substrates." J Am Chem Soc **137**(20): 6418-6427.

Chen, H. Y., P. E. Z. Larson, R. A. Bok, C. von Morze, R. Sriram, R. Delos Santos, J. Delos Santos, J. W. Gordon, N. Bahrami, M. Ferrone, J. Kurhanewicz and D. B. Vigneron (2017). "Assessing Prostate Cancer Aggressiveness with Hyperpolarized Dual-Agent 3D Dynamic Imaging of Metabolism and Perfusion." Cancer Res **77**(12): 3207-3216.

Chirindel, A., K. C. Alluri, M. A. Chaudhry, R. L. Wahl, T. M. Pawlik, J. M. Herman and R. M. Subramaniam (2015). "Prognostic Value of FDG PET/CT-Derived Parameters in Pancreatic Adenocarcinoma at Initial PET/CT Staging." AJR Am J Roentgenol **204**(5): 1093-1099.

Clark, C. E., S. R. Hingorani, R. Mick, C. Combs, D. A. Tuveson and R. H. Vonderheide (2007). "Dynamics of the Immune Reaction to Pancreatic Cancer from Inception to Invasion." Cancer Research **67**(19): 9518-9527.

Collisson, E. A., P. Bailey, D. K. Chang and A. V. Biankin (2019). "Molecular subtypes of pancreatic cancer." Nat Rev Gastroenterol Hepatol **16**(4): 207-220.

Collisson, E. A., A. Sadanandam, P. Olson, W. J. Gibb, M. Truitt, S. Gu, J. Cooc, J. Weinkle, G. E. Kim, L. Jakkula, H. S. Feiler, A. H. Ko, A. B. Olshen, K. L. Danenberg, M. A. Tempero, P. T. Spellman, D. Hanahan and J. W. Gray (2011). "Subtypes of pancreatic ductal adenocarcinoma and their differing responses to therapy." Nature Medicine **17**: 500.

Comment, A. and M. E. Merritt (2014). "Hyperpolarized magnetic resonance as a sensitive detector of metabolic function." Biochemistry **53**(47): 7333-7357.

Conroy, T., P. Hammel, M. Hebbar, M. Ben Abdelghani, A. C. Wei, J. L. Raoul, L. Chone, E. Francois, P. Artru, J. J. Biagi, T. Lecomte, E. Assenat, R. Faroux, M. Ychou, J. Volet, A. Sauvanet, G. Breysacher, F. Di Fiore, C. Cripps, P. Kavan, P. Texereau, K. Bouhier-Leporrier, F. Khemissa-Akouz, J. L. Legoux, B. Juzyna, S. Gourgou, C. J. O'Callaghan, C. Jouffroy-Zeller, P. Rat, D. Malka, F. Castan, J. B. Bachet, G. Canadian Cancer Trials and G. I. P. G. the Unicancer (2018). "FOLFIRINOX or Gemcitabine as Adjuvant Therapy for Pancreatic Cancer." N Engl J Med **379**(25): 2395-2406.

Daemen, A., D. Peterson, N. Sahu, R. McCord, X. Du, B. Liu, K. Kowanetz, R. Hong, J. Moffat, M. Gao, A. Boudreau, R. Mroue, L. Corson, T. O'Brien, J. Qing, D. Sampath, M. Merchant, R. Yauch, G. Manning, J. Settleman, G. Hatzivassiliou and M. Evangelista (2015). "Metabolite profiling stratifies pancreatic ductal adenocarcinomas into subtypes with distinct sensitivities to metabolic inhibitors." Proc Natl Acad Sci U S A **112**(32): E4410-4417.

Day, S. E., M. I. Kettunen, F. A. Gallagher, D. E. Hu, M. Lerche, J. Wolber, K. Golman, J. H. Ardenkjaer-Larsen and K. M. Brindle (2007). "Detecting tumor response to treatment using hyperpolarized 13C magnetic resonance imaging and spectroscopy." Nat Med **13**(11): 1382-1387.

Dong, Y., R. Eskandari, C. Ray, K. L. Granlund, L. D. Santos-Cunha, V. Z. Miloushev, S. S. Tee, S. Jeong, O. Aras, Y. B. Chen, E. H. Cheng, J. J. Hsieh and K. R. Keshari (2019). "Hyperpolarized MRI Visualizes Warburg Effects and Predicts Treatment Response to mTOR Inhibitors in Patient-Derived ccRCC Xenograft Models." Cancer Res **79**(1): 242-250.

Dutta, P., M. R. Perez, J. Lee, Y. Kang, M. Pratt, T. C. Salzillo, J. Weygand, N. M. Zacharias, S. T. Gammon, E. J. Koay, M. Kim, F. McAllister, S. Sen, A. Maitra, D. Piwnica-Worms, J. B. Fleming and P. K. Bhattacharya (2019). "Combining Hyperpolarized Real-Time Metabolic

Imaging and NMR Spectroscopy To Identify Metabolic Biomarkers in Pancreatic Cancer." J Proteome Res **18**(7): 2826-2834.

Ferro, R. and M. Falasca (2014). "Emerging role of the KRAS-PDK1 axis in pancreatic cancer." World J Gastroenterol **20**(31): 10752-10757.

Fukukura, Y., T. Shindo, H. Hakamada, K. Takumi, T. Umanodan, M. Nakajo, K. Kamimura, A. Umanodan, J. Ideue and T. Yoshiura (2016). "Diffusion-weighted MR imaging of the pancreas: optimizing b-value for visualization of pancreatic adenocarcinoma." Eur Radiol **26**(10): 3419-3427.

Gallagher, F. A., R. Woitek, M. A. McLean, A. B. Gill, R. Manzano Garcia, E. Provenzano, F. Riemer, J. Kaggie, A. Chhabra, S. Ursprung, J. T. Grist, C. J. Daniels, F. Zaccagna, M. C. Laurent, M. Locke, S. Hilborne, A. Frary, T. Torheim, C. Boursnell, A. Schiller, I. Patterson, R. Slough, B. Carmo, J. Kane, H. Biggs, E. Harrison, S. S. Deen, A. Patterson, T. Lanz, Z. Kingsbury, M. Ross, B. Basu, R. Baird, D. J. Lomas, E. Sala, J. Wason, O. M. Rueda, S. F. Chin, I. B. Wilkinson, M. J. Graves, J. E. Abraham, F. J. Gilbert, C. Caldas and K. M. Brindle (2020). "Imaging breast cancer using hyperpolarized carbon-13 MRI." Proc Natl Acad Sci U S A **117**(4): 2092-2098.

Goonetilleke, K. S. and A. K. Siriwardena (2007). "Systematic review of carbohydrate antigen (CA 19-9) as a biochemical marker in the diagnosis of pancreatic cancer." European Journal of Surgical Oncology **33**(3): 266-270.

Grasso, C., G. Jansen and E. Giovannetti (2017). "Drug resistance in pancreatic cancer: Impact of altered energy metabolism." Critical Reviews in Oncology/Hematology **114**(Supplement C): 139-152.

Heid, I., K. Steiger, M. Trajkovic-Arsic, M. Settles, M. R. Esswein, M. Erkan, J. Kleeff, C. Jager, H. Friess, B. Haller, A. Steingotter, R. M. Schmid, M. Schwaiger, E. J. Rummeny, I. Esposito, J. T. Siveke and R. F. Braren (2017). "Co-clinical Assessment of Tumor Cellularity in Pancreatic Cancer." Clin Cancer Res **23**(6): 1461-1470.

Hesketh, R. L. and K. M. Brindle (2018). "Magnetic resonance imaging of cancer metabolism with hyperpolarized (13)C-labeled cell metabolites." Curr Opin Chem Biol **45**: 187-194.

Hidalgo , M. (2010). "Pancreatic Cancer." New England Journal of Medicine **362**(17): 1605-1617.

Hill, D. K., Y. Jamin, M. R. Orton, N. Tardif, H. G. Parkes, S. P. Robinson, M. O. Leach, Y. L. Chung and T. R. Eykyn (2013). "(1)H NMR and hyperpolarized (1)(3)C NMR assays of pyruvate-lactate: a comparative study." NMR Biomed **26**(10): 1321-1325.

Hingorani, S. R., L. Zheng, A. J. Bullock, T. E. Seery, W. P. Harris, D. S. Sigal, F. Braiteh, P. S. Ritch, M. M. Zalupski, N. Bahary, P. E. Oberstein, A. Wang-Gillam, W. Wu, D. Chondros, P. Jiang, S. Khelifa, J. Pu, C. Aldrich and A. E. Hendifar (2018). "HALO 202: Randomized Phase II Study of PEGPH20 Plus Nab-Paclitaxel/Gemcitabine Versus Nab-Paclitaxel/Gemcitabine in Patients With Untreated, Metastatic Pancreatic Ductal Adenocarcinoma." Journal of Clinical Oncology **36**(4): 359-366.

Hruban, R. H., M. Goggins, J. Parsons and S. E. Kern (2000). "Progression Model for Pancreatic Cancer." Clinical Cancer Research **6**(8): 2969-2972.

Hundshammer, C., M. Braeuer, C. A. Muller, A. E. Hansen, M. Schillmaier, S. Duwel, B. Feuerecker, S. J. Glaser, A. Haase, W. Weichert, K. Steiger, J. Cabello, F. Schilling, J. B. Hovener, A. Kjaer, S. G. Nekolla and M. Schwaiger (2018). "Simultaneous characterization of tumor cellularity and the Warburg effect with PET, MRI and hyperpolarized (13)C-MRSI." Theranostics **8**(17): 4765-4780.

Hundshammer, C., S. Duwel, D. Ruseckas, G. Topping, P. Dzien, C. Muller, B. Feuerecker, J. B. Hovener, A. Haase, M. Schwaiger, S. J. Glaser and F. Schilling (2018). "Hyperpolarized Amino Acid Derivatives as Multivalent Magnetic Resonance pH Sensor Molecules." Sensors (Basel) **18**(2).

Ichikawa, T., S. M. Erturk, U. Motosugi, H. Sou, H. Iino, T. Araki and H. Fujii (2007). "High-b value diffusion-weighted MRI for detecting pancreatic adenocarcinoma: preliminary results." AJR Am J Roentgenol **188**(2): 409-414.

International Agency for Research on Cancer, W. H. O. (2018). "Global Cancer Observatory 2018."

Jacobetz, M. A., D. S. Chan, A. Neesse, T. E. Bapiro, N. Cook, K. K. Frese, C. Feig, T. Nakagawa, M. E. Caldwell, H. I. Zecchini, M. P. Lolkema, P. Jiang, A. Kultti, C. B. Thompson, D. C. Maneval, D. I. Jodrell, G. I. Frost, H. M. Shepard, J. N. Skepper and D. A. Tuveson (2013). "Hyaluronan impairs vascular function and drug delivery in a mouse model of pancreatic cancer." Gut **62**(1): 112-120.

Jendoubi, S., M. Wagner, S. Montagne, M. Ezziane, J. Mespoulet, E. Comperat, C. Estellat, A. Baptiste and R. Renard-Penna (2019). "MRI for prostate cancer: can computed high b-value DWI replace native acquisitions?" Eur Radiol **29**(10): 5197-5204.

Jeune, F., R. Coriat, F. Prat, B. Dousset, J. C. Vaillant and S. Gaujoux (2019). "Pancreatic cancer surgical management." Presse Med **48**(3 Pt 2): e147-e158.

Kaissis, G. and R. Braren (2019). "Pancreatic cancer detection and characterization-state of the art cross-sectional imaging and imaging data analysis." Transl Gastroenterol Hepatol **4**: 35.

Kaissis, G., S. Ziegelmayer, F. Lohofer, H. Algul, M. Eiber, W. Weichert, R. Schmid, H. Friess, E. Rummeny, D. Ankerst, J. Siveke and R. Braren (2019). "A machine learning model for the prediction of survival and tumor subtype in pancreatic ductal adenocarcinoma from preoperative diffusion-weighted imaging." Eur Radiol Exp **3**(1): 41.

Kaissis, G., S. Ziegelmayer, F. Lohofer, K. Steiger, H. Algul, A. Muckenhuber, H. Y. Yen, E. Rummeny, H. Friess, R. Schmid, W. Weichert, J. T. Siveke and R. Braren (2019). "A machine learning algorithm predicts molecular subtypes in pancreatic ductal adenocarcinoma with differential response to gemcitabine-based versus FOLFIRINOX chemotherapy." PLoS One **14**(10): e0218642.

Kalimuthu, N., G. W. Wilson, R. C. Grant, M. Seto, G. O'Kane, R. Vajpeyi, F. Notta, S. Gallinger and R. Chetty (2020). "Morphological classification of pancreatic ductal adenocarcinoma that predicts molecular subtypes and correlates with clinical outcome." Gut **69**(2): 317-328.

Kanda, M., H. Matthaei, J. Wu, S. M. Hong, J. Yu, M. Borges, R. H. Hruban, A. Maitra, K. Kinzler, B. Vogelstein and M. Goggins (2012). "Presence of somatic mutations in most early-stage pancreatic intraepithelial neoplasia." Gastroenterology **142**(4): 730-733 e739.

Khan, M., S. Azim, H. Zubair, A. Bhardwaj, G. Patel, M. d. Khushman, S. Singh and A. Singh (2017). "Molecular Drivers of Pancreatic Cancer Pathogenesis: Looking Inward to Move Forward." International Journal of Molecular Sciences **18**(4): 779.

Klöppel, G. and J. Lüttges (2001). "WHO-classification 2000: exocrine pancreatic tumors." Verhandlungen der Deutschen Gesellschaft fur Pathologie **85**: 219-228.

Koh, D.-M. and D. J. Collins (2007). "Diffusion-Weighted MRI in the Body: Applications and Challenges in Oncology." American Journal of Roentgenology **188**(6): 1622-1635.

Lodi, A., S. M. Woods and S. M. Ronen (2013). "Treatment with the MEK inhibitor U0126 induces decreased hyperpolarized pyruvate to lactate conversion in breast, but not prostate, cancer cells." NMR Biomed **26**(3): 299-306.

Mallet, R. T., A. H. Olivencia-Yurvati and R. Bunger (2018). "Pyruvate enhancement of cardiac performance: Cellular mechanisms and clinical application." Exp Biol Med (Maywood) **243**(2): 198-210.

McGuigan, A., P. Kelly, R. C. Turkington, C. Jones, H. G. Coleman and R. S. McCain (2018). "Pancreatic cancer: A review of clinical diagnosis, epidemiology, treatment and outcomes." World J Gastroenterol **24**(43): 4846-4861.

Miquel Porta, X. F., Núria Malats, Luisa Guarner, Alfredo Carrato, Ana de Miguel, Laura Ruiz, Manuel Jariod, Sergi Costafreda, Susana Coll, Juan Alguacil, Josep M Corominas, Ricard Solà, Antonio Salas, Francisco X Real (2005). "Exocrine Pancreatic Cancer: Symptoms at Presentation and Their Relation to Tumour Site and Stage." Clin Transl Oncol.

Moffitt, R. A., R. Marayati, E. L. Flate, K. E. Volmar, S. G. Loeza, K. A. Hoadley, N. U. Rashid, L. A. Williams, S. C. Eaton, A. H. Chung, J. K. Smyla, J. M. Anderson, H. J. Kim, D. J. Bentrem, M. S. Talamonti, C. A. Iacobuzio-Donahue, M. A. Hollingsworth and J. J. Yeh (2015). "Virtual microdissection identifies distinct tumor- and stroma-specific subtypes of pancreatic ductal adenocarcinoma." Nat Genet **47**(10): 1168-1178.

Morton, J. P., S. A. Karim, K. Graham, P. Timpson, N. Jamieson, D. Athineos, B. Doyle, C. McKay, M. Y. Heung, K. A. Oien, M. C. Frame, T. R. J. Evans, O. J. Sansom and V. G. Brunton "Dasatinib Inhibits the Development of Metastases in a Mouse Model of Pancreatic Ductal Adenocarcinoma." Gastroenterology **139**(1): 292-303.

Muckenhuber, A., A. K. Berger, A. M. Schlitter, K. Steiger, B. Konukiewitz, A. Trumpp, R. Eils, J. Werner, H. Friess, I. Esposito, G. Kloppel, G. O. Ceyhan, M. Jesinghaus, C. Denkert, M. Bahra, A. Stenzinger, M. R. Sprick, D. Jager, C. Springfeld and W. Weichert (2018). "Pancreatic Ductal Adenocarcinoma Subtyping Using the Biomarkers Hepatocyte Nuclear Factor-1A and Cytokeratin-81 Correlates with Outcome and Treatment Response." Clin Cancer Res **24**(2): 351-359.

Neil, J. J. (1997). "Measurement of water motion (apparent diffusion) in biological systems." Concepts in Magnetic Resonance **9**(6): 385-401.

Olive, K. P., M. A. Jacobetz, C. J. Davidson, A. Gopinathan, D. McIntyre, D. Honess, B. Madhu, M. A. Goldgraben, M. E. Caldwell, D. Allard, K. K. Frese, G. DeNicola, C. Feig, C. Combs, S. P. Winter, H. Ireland-Zecchini, S. Reichelt, W. J. Howat, A. Chang, M. Dhara, L. Wang, F. Rückert, R. Grützmann, C. Pilarsky, K. Izeradjene, S. R. Hingorani, P. Huang, S. E. Davies, W. Plunkett, M. Egorin, R. H. Hruban, N. Whitebread, K. McGovern, J. Adams, C. Iacobuzio-Donahue, J. Griffiths and D. A. Tuveson (2009). "Inhibition of Hedgehog Signaling Enhances Delivery of Chemotherapy in a Mouse Model of Pancreatic Cancer." Science **324**(5933): 1457-1461.

Porter, R. L., N. K. C. Magnus, V. Thapar, R. Morris, A. Szabolcs, A. Neyaz, A. S. Kulkarni, E. Tai, A. Chougule, A. Hillis, G. Golczer, H. Guo, T. Yamada, T. Kurokawa, C. Yashaswini, M. Ligorio, K. D. Vo, L. Nieman, A. S. Liss, V. Deshpande, M. S. Lawrence, S. Maheswaran, C. Fernandez-Del Castillo, T. S. Hong, D. P. Ryan, P. J. O'Dwyer, J. A. Drebin, C. R. Ferrone, D. A. Haber and D. T. Ting (2019). "Epithelial to mesenchymal plasticity and differential response to therapies in pancreatic ductal adenocarcinoma." Proc Natl Acad Sci U S A.

Provenzano, Paolo P., C. Cuevas, Amy E. Chang, Vikas K. Goel, Daniel D. Von Hoff and Sunil R. Hingorani (2012). "Enzymatic Targeting of the Stroma Ablates Physical Barriers to Treatment of Pancreatic Ductal Adenocarcinoma." Cancer Cell **21**(3): 418-429.

Rahib, L., B. D. Smith, R. Aizenberg, A. B. Rosenzweig, J. M. Fleshman and L. M. Matrisian (2014). "Projecting cancer incidence and deaths to 2030: the unexpected burden of thyroid, liver, and pancreas cancers in the United States." Cancer Res **74**(11): 2913-2921.

Rajeshkumar, N. V., P. Dutta, S. Yabuuchi, R. F. de Wilde, G. V. Martinez, A. Le, J. J. Kamphorst, J. D. Rabinowitz, S. K. Jain, M. Hidalgo, C. V. Dang, R. J. Gillies and A. Maitra (2015). "Therapeutic Targeting of the Warburg Effect in Pancreatic Cancer Relies on an Absence of p53 Function." Cancer Res **75**(16): 3355-3364.

Rong, Y., W. Wu, X. Ni, T. Kuang, D. Jin, D. Wang and W. Lou (2013). "Lactate dehydrogenase A is overexpressed in pancreatic cancer and promotes the growth of pancreatic cancer cells." Tumour Biol **34**(3): 1523-1530.

Ros, S., A. J. Wright, P. D'Santos, D. E. Hu, R. L. Hesketh, Y. Lubling, D. Georgopoulou, G. Lerda, D. L. Couturier, P. Razavi, R. Pelossof, A. S. Batra, E. Mannion, D. Y. Lewis, A. Martin,

R. D. Baird, M. Oliveira, L. W. de Boo, S. C. Linn, M. Scaltriti, O. M. Rueda, A. Bruna, C. Caldas and K. M. Brindle (2020). "Metabolic Imaging Detects Resistance to PI3Kalpha Inhibition Mediated by Persistent FOXM1 Expression in ER(+) Breast Cancer." Cancer Cell **38**(4): 516-533 e519.

Rosty, C. and M. Goggins (2002). "Early detection of pancreatic carcinoma." Hematol Oncol Clin North Am **16**(1): 37-52.

Satake, K., G. Kanazawa, I. Kho, Y. Chung and K. Umeyama (1985). "Evaluation of serum pancreatic enzymes, carbohydrate antigen 19-9, and carcinoembryonic antigen in various pancreatic diseases." Am J Gastroenterol **80**(8): 630-636.

Serrao, E. M., M. I. Kettunen, T. B. Rodrigues, P. Dzien, A. J. Wright, A. Gopinathan, F. A. Gallagher, D. Y. Lewis, K. K. Frese, J. Almeida, W. J. Howat, D. A. Tuveson and K. M. Brindle (2016). "MRI with hyperpolarised [1-13C]pyruvate detects advanced pancreatic preneoplasia prior to invasive disease in a mouse model." Gut **65**(3): 465-475.

Siegel, R. L., K. D. Miller and A. Jemal (2020). "Cancer statistics, 2020." CA Cancer J Clin **70**(1): 7-30.

Siveke, J. T., H. Einwächter, B. Sipos, C. Lubeseder-Martellato, G. Klöppel and R. M. Schmid (2007). "Concomitant Pancreatic Activation of KrasG12D and Tgfa Results in Cystic Papillary Neoplasms Reminiscent of Human IPMN." Cancer Cell **12**(3): 266-279.

Stejskal, E. O. and J. E. Tanner (1965). "Spin Diffusion Measurements: Spin Echoes in the Presence of a Time-Dependent Field Gradient." The Journal of Chemical Physics **42**(1): 288-292.

Toft, J., W. J. Hadden, J. M. Laurence, V. Lam, L. Yuen, A. Janssen and H. Pleass (2017). "Imaging modalities in the diagnosis of pancreatic adenocarcinoma: A systematic review and meta-analysis of sensitivity, specificity and diagnostic accuracy." Eur J Radiol **92**: 17-23.

Topping, G. J., C. Hundshammer, L. Nagel, M. Grashei, M. Aigner, J. G. Skinner, R. F. Schulte and F. Schilling (2020). "Acquisition strategies for spatially resolved magnetic resonance detection of hyperpolarized nuclei." MAGMA **33**(2): 221-256.

Torphy, R. J., Z. Wang, A. True-Yasaki, K. E. Volmar, N. Rashid, B. Yeh, J. M. Anderson, J. S. Johansen, M. A. Hollingsworth, J. J. Yeh and E. A. Collisson (2018). "Stromal Content Is

Correlated With Tissue Site, Contrast Retention, and Survival in Pancreatic Adenocarcinoma." JCO Precis Oncol **2018**.

Trajkovic-Arsic, M., I. Heid, K. Steiger, A. Gupta, A. Fingerle, C. Worner, N. Teichmann, S. Sengkwawoh-Lueong, P. Wenzel, A. J. Beer, I. Esposito, R. Braren and J. T. Siveke (2017). "Apparent Diffusion Coefficient (ADC) predicts therapy response in pancreatic ductal adenocarcinoma." Sci Rep **7**(1): 17038.

Warburg, O. (1956). "On the Origin of Cancer Cells." Science **123**(3191): 309-314.

Weissmueller, S., E. Manchado, M. Saborowski, J. P. t. Morris, E. Wagenblast, C. A. Davis, S. H. Moon, N. T. Pfister, D. F. Tschaharganeh, T. Kitzing, D. Aust, E. K. Markert, J. Wu, S. M. Grimmond, C. Pilarsky, C. Prives, A. V. Biankin and S. W. Lowe (2014). "Mutant p53 drives pancreatic cancer metastasis through cell-autonomous PDGF receptor beta signaling." Cell **157**(2): 382-394.

Wong, K. M., K. J. Horton, A. L. Coveler, S. R. Hingorani and W. P. Harris (2017). "Targeting the Tumor Stroma: the Biology and Clinical Development of Pegylated Recombinant Human Hyaluronidase (PEGPH20)." Current Oncology Reports **19**(7): 47.

Zachar, Z., J. Marecek, C. Maturo, S. Gupta, S. D. Stuart, K. Howell, A. Schauble, J. Lem, A. Piramzadian, S. Karnik, K. Lee, R. Rodriguez, R. Shorr and P. M. Bingham (2011). "Non-redox-active lipoate derivates disrupt cancer cell mitochondrial metabolism and are potent anticancer agents in vivo." J Mol Med (Berl) **89**(11): 1137-1148.

Acknowledgements

I would like to thank PD Dr. Rickmer Braren for the opportunity to work in his team and gain an inside experience of experimental radiology. It was an honor and a pleasure to work in his team.

Without Dr. Irina Heid this thesis would not have been possible. Thank you for always helping me out, with words and deeds.

Thanks to the Department of Nuclear Medicine and Prof. Dr. Franz Schilling for the fact that we were allowed to use the equipment and the many ideas and suggestions for improvement to our experiments. I would also like to thank for the custom data analysis software, written in Matlab, which was used for the data analysis.

I would also like to thank Dr. Geoffrey Toppings for his patience and the many hours that we spent together at the MRI.

A big thank you to Iryna Skuratvoska for the great help in the laboratory and helping me with the genotyping and cell preparations. I would also like to thank Elisabeth Bliemsrieder for helping me with the cell preparations for the rat experiments.

A very important person who always gave me support during this time was Luisa, thank you for always being there for me.

Last but not least I would like to thank my family for always supporting me during my studies and the writing of this thesis.